Mathematical derivation and verification of LISA's angular readout signal on an ultrastable interferometer testbed

Alvise Pizzella,[*] Miguel Dovale-Álvarez,[†] Pablo Martínez Cano, Rodrigo García Álvarez, Christoph Bode, Juan José Esteban Delgado, and Gerhard Heinzel[‡]

Max Planck Institute for Gravitational Physics (Albert Einstein Institute), D-30167 Hannover, Germany and Leibniz Universität Hannover, D-30167 Hannover, Germany

(Received 24 June 2025; accepted 30 September 2025; published 28 October 2025; corrected 20 January 2026)

The Laser Interferometer Space Antenna (LISA) aims to detect gravitational waves by interferometrically measuring the separation between free falling test masses (TMs) with pm/$\sqrt{\text{Hz}}$ sensitivity down to mHz frequencies. Achieving this sensitivity requires the suppression of spurious path length variations induced by unavoidable tilts of the TMs and spacecraft, a phenomenon known as tilt-to-length coupling. LISA employs differential wave front sensing (DWS) to measure angular misalignments between the interfering beams' wave fronts. To first-order approximation, the DWS signal is linearly dependent on the tilt angle for small angular displacements (on the order of microradians). The linear coupling coefficient is well-documented for the idealized case of a photodiode (PD) much larger than the beam spot radius. However, LISA's setup violates this assumption, and the anticipated tilt range exceeds the linear regime. Accurately characterizing the DWS signal thus requires a more comprehensive approach. This paper presents a novel analytical framework for calculating the first two Maclaurin coefficients of the DWS signal for two fundamental-mode Gaussian beams with a small wave front curvature mismatch, incident on PDs of arbitrary size. The validity of this approach is verified by comparison with numerical simulations and experimental calibrations conducted on an ultrastable testbed representative of LISA. Moreover, we utilize this framework to determine the phase sensitivity required to meet LISA's stringent measurement requirements. The results of this paper will facilitate the calculation of the DWS gain of an interferometric topology and give a reference target to the experiments aiming to demonstrate LISA's performance requirement.

DOI: 10.1103/sqgt-plx6

I. INTRODUCTION

The quest for the detection of gravitational waves began with Joseph Weber at the University of Maryland in the early sixties, using resonant bars at room temperature [1]. This first generation of detectors was followed by a second generation of cryogenic resonant bar detectors, which operated between 1985 and 2010 [1]. Unfortunately, these failed to obtain strong enough evidence to claim a detection. The alternative technology of laser interferometry for gravitational wave detection was also proposed by Weber [2]. The foundations for its use in the Laser Interferometer Gravitational-Wave Observatory (LIGO) were established by Rainer Weiss in [3].

Finally, on 14 September 2015, the LIGO experiment, a second-generation laser interferometer sensitive in the Hz–kHz band, made the first detection of a gravitational wave signal originating from a binary black hole merger, later named event GW150914 [4]. This result has consolidated the use of laser interferometry between free falling test masses (TMs) as a suitable technology for detecting gravitational waves and incentivized its further exploitation. While a third generation of ground-based gravitational wave interferometers, as Einstein Telescope [5] and Cosmic Explorer [6], is on the way, the bandwidth of these detectors is limited in the low-end by Newtonian noise [7]. Detecting the sub-Hz gravitational wave signals requires spaceborne interferometric detectors such as the LISA.

The LISA mission will allow us to probe a rich and yet unexplored band of the gravitational universe, covering frequencies between 0.1 mHz and 1 Hz. The mission was adopted by the European Space Agency (ESA) in 2024 [8]. Key parts of the required technology—free falling TMs local interferometry—was successfully tested in the LISA

[*]Contact author: alvise.pizzella@aei.mpg.de
[†]Contact author: miguel.dovale@aei.mpg.de
[‡]Contact author: gerhard.heinzel@aei.mpg.de

Published by the American Physical Society under the terms of the Creative Commons Attribution 4.0 International license. Further distribution of this work must maintain attribution to the author(s) and the published article's title, journal citation, and DOI. Open access publication funded by the Max Planck Society.

Pathfinder (LPF) mission, which was launched on 3 December 2015 also by ESA [9–11]. Still, LISA's interferometer features the longest baseline of any experiment in history, as the separation between the spacecraft is approximately 2.5 million kilometers. Achieving the precision necessary to detect gravitational waves—of the order of $\mathrm{pm}/\sqrt{\mathrm{Hz}}$—over this baseline cannot be fully tested prior to the mission. This detection scheme presents unique challenges that require detailed characterization beforehand.

LISA uses heterodyne interferometry to probe the separation between free falling test masses (TMs), which are shielded from external disturbances by their host spacecraft. The TM-to-TM measurement is split into three submeasurements:

(i) a TM to spacecraft separation measurement in the starting spacecraft, called test mass interferometer (TMI);
(ii) a spacecraft to spacecraft measurement, called intersatellite interferometer (ISI);
(iii) a second TMI in the final spacecraft.

An additional reference interferometer (RFI) is present as a phase reference [12].

In the ISI, a Gaussian beam (Rx) is transmitted by the transmitting spacecraft via a telescope and propagates for $\sim 2.5 \times 10^9$ m until it is received by another, equal telescope in the receiving spacecraft. During this ~8.3 second journey, the beam diverges into a several-kilometer-wide profile, of which only a small portion is clipped by the receiving telescope. The received beam is interfered with a local beam (Tx), producing a heterodyne beatnote that encodes the relative phase variations containing the gravitational-wave signal. Interference for both the TMI and the ISI (as well as the RFI) occurs on the LISA-optical bench (LOB) [13], the main component of LISA's optical metrology system. The LOB comprises an ultra-low-expansion glass baseplate to which optical elements are bonded via hydroxide-catalysis bonding [14], forming LISA's interferometers. Each spacecraft hosts two LOBs.

The path length measurement required to probe the TM to TM displacement is affected by numerous noise sources at different levels, such as the instrumental level and the optical link level. The main optical noise is laser frequency noise, which is suppressed by a technique named time delayed interferometry (TDI) [15]. Tilt-to-length (TTL) coupling, which was a dominating noise source also in LPF [16], is, according to recent estimates, one of the most significant contributions to the total noise budget in LISA. The unavoidable jitter of the TMs with respect to the spacecraft, between components in the spacecraft and of the spacecraft itself contribute significantly to the overall noise in the interferometric displacement measurement. In LISA, the main tilt sources have a well-defined pivot, which allows the use of imaging systems to suppress TTL. The tilts of the spacecraft are imaged by the telescope into an aperture located on the LOB which is named Rx-clip, making it the effective tilt pivot of the Rx beam on the LOB. The tilts of the TMs have the surface of the TM itself as tilt pivot.

In LISA, TTL is expected to affect mainly the ISI. To mitigate such coupling of tilts into the optically measured path length s, LISA employs a three-fold strategy:

(i) the attitudes of the spacecraft and of the TMs are actively controlled by a system named Drag-Free and Attitude Control System (DFACS). This system has the purpose of ensuring the free fall of the TMs and satellite pointing; by doing so, it also mitigates the overall jitter in the interferometer.
(ii) the TTL coupling is *passively* reduced through the use of imaging systems (see subsection II D), as demonstrated by the testbed described in Sec. II of this article for both Gaussian-to-Gaussian beam [17] and flat-top-to-Gaussian beam interference [18].
(iii) the extra pathlength Δs caused by the tilts—expressed as $\Delta s = \Delta s(\varphi, \eta)$, where φ and η denote the yaw and pitch angles—is modeled and subtracted during *postprocessing* by measuring these tilt angles [19].

Both the postprocessing mitigation and DFACS require an angular readout of the TM's orientation relative to the spacecraft and also of the LOB/spacecraft with respect to the line of sight to the other spacecraft with a precision on the order of 1 $\mathrm{nrad}/\sqrt{\mathrm{Hz}}$ in the LISA detection band. This readout is provided by a technique known as differential wave front sensing (DWS), which is described in Sec. II G. The calibration of this technique can be derived from the geometrical parameters of the setup, although this derivation is nontrivial.

This article presents an investigation into the calibration of the DWS signal. The DWS signal is a complicated odd function of the beam tilt angle. For small tilts $\mathcal{O}(\mu\mathrm{rad})$, the calibration is linear, and the proportionality coefficient is known, in the limit of a photodiode (PD) much larger than the beam in size. Neither condition applies to LISA, as the tilts will exceed the linear regime, and the beam size is comparable to that of the PD.

A full calculation of the DWS signal typically requires numerical methods, since the involved integrals cannot be solved analytically. In this article, however, the calculation is approached analytically by employing justified approximations. This yields first- and third-order Maclaurin coefficients, which are nontrivial functions of geometrical parameters of the interferometrical topology, including the laser wavelength, the beams' sizes and radius of curvature (RoC) and the PD's size.

These results are then compared to an experimentally realized DWS calibration realized on an ultrastable testbed representative of LISA. The analytical and numerical results are finally used to translate ESA's angular readout requirements for LISA into corresponding phase noise requirements.

Section II presents the measurement concept and the layout of the testbed used for the experimental verification of the DWS calibration and its relevant subsystems. Section III presents an introduction to DWS and the derivation of the DWS signal under various assumptions. Section IV presents a derivation of how the DWS signal is influenced by the use of imaging systems. Section V provides the experimental results and the calibrated DWS signals. Finally, Sec. VI presents a derivation of the phase readout noise which has to be met by a testbed in order to demonstrate the DWS and longitudinal path length signal (LPS) performance level for LISA.

II. SETUP

A. Overview of the testbed

A testbed to simulate the above described effects on the LOB was developed by the authors of [20]. The TTL coupling and DWS Optical Bench Simulator (TDOBS) testbed was designed with the primary purpose of demonstrating, in a LISA-representative manner, that imaging systems can be used to suppress TTL coupling [20]. Additionally, TDOBS has been designed as a versatile platform for testing of other aspects of LISA metrology, such as imaging systems, photoreceivers, and mechanisms to compensate linear TTL [20]. The optical layout of the testbed is shown in Fig. 1.

The layout consists of two Zerodur® glass-ceramic baseplates: the optical bench (OB) and the telescope simulator (TS). The OB is a simplified version of the LOB, featuring only one interferometer capable of simulating either of LISA's three interferometers. The TS is an optical ground support equipment which sits on top of the OB and provides it with beams which are representative of either the TMI (a tilting Gaussian-beam) or the ISI (a tilting flattop beam). These beams are named Rx Gaussian-beam (Rx-GB) and Rx flattop (Rx-FT), respectively.

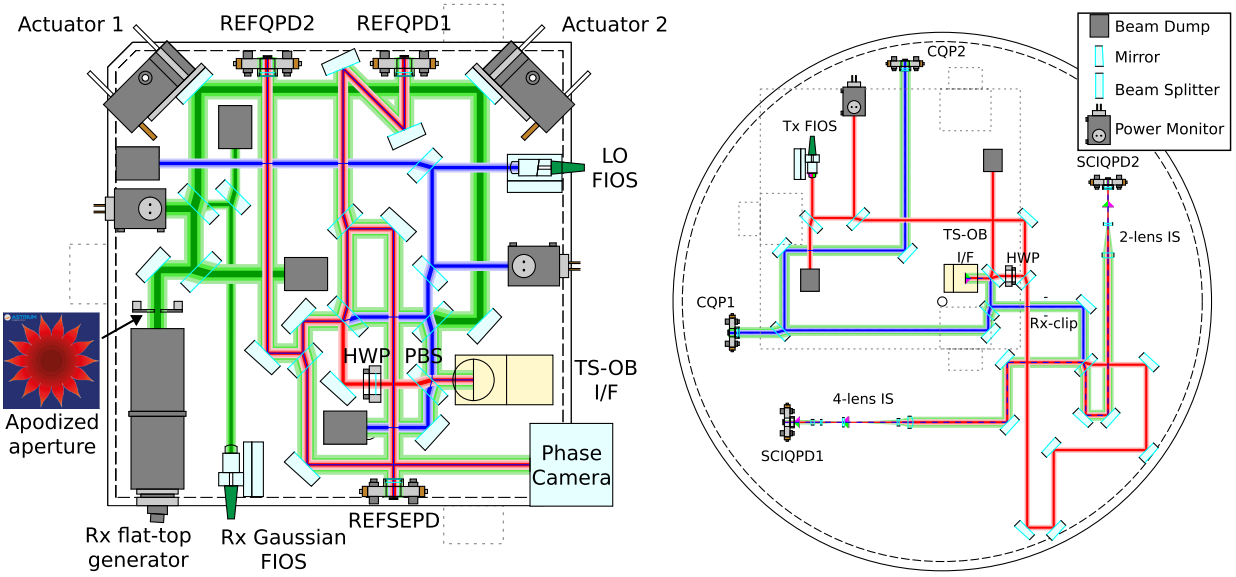

FIG. 1. Optical layout of the testbed. Left: The telescope simulator (TS) provides the optical bench (OB) with laser beams (Rx-GB and Rx-FT, both in green) to simulate LISA's TMI and ISI. The first beam is a Gaussian beam provided by a fiber injector optical subassembly (FIOS) with a width of ∼2 mm. The second is a flattop beam generated by clipping a 9 mm radius beam radius Gaussian beam on an apodized aperture; this generates a beam flat in both intensity and phase with a diameter of ∼4 mm [20]. The TS sits on top of the OB and is held by three Zerodur® feet, which are indicated by the dashed lines. An optical link is established via a vertical interface (TS/OB I/F). A pair of actuated steering mirrors on the TS tilt the Rx beams around the Rx-clip (this is an aperture, which is physically located on the LOB) to simulate either the spacecraft jitter in the ISI of the TM jitter on the TMI. An additional beam, the LO (blue), is used as an alignment aid for the TS with respect to the OB and as a phase reference. The TS hosts four optical copies of the Rx-clip (located on the OB). In these optical copies, one reference SEPD (REFSEPD), two reference QPDs (REFQPDs) and a phase camera are placed. Right: The OB is a simplified version of the OBs in LISA. It features only one interferometer, where all three the Tx, Rx, and the LO beams interfere. At the interferometer's two output ports, the two science QPDs (SCIQPDs) are placed. These output ports feature imaging systems to image the point of rotation of the Rx beam onto the center of the QPDs and reduce TTL coupling. In this figure we show the two types of imaging systems that were developed for TDOBS, one featuring two lenses, and one featuring four lenses. During the work reported in this article, two 4-lense imaging systems were used. The TS's nominal position on top of the OB is indicated by the dashed lines. Such position is defined with the aid of a Calibrated QPD Pair (CQP); this is a pair of large silicon QPDs positioned on the LOB. When the LO beam impinges on the center of both QPDs of the CQP, the Tx beam TS also propagates to the center of the PDs on the TS.

A pair of steering mirrors on the TS enables the synthesis of beam tilts representative of either the TM tilt or the spacecraft tilt. The testbed has recently been upgraded to the use of beat notes in a frequency range of 5–25 MHz (the LISA heterodyne band) and with low noise photoreceiver (PR) representative of those used in LISA [21].

B. Laser modulation bench

The laser modulation bench generates and delivers three beams [Rx, Local Oscillator (LO) and Tx] to TDOBS. All three originate from a single laser source: an NPRO-type Nd:YAG 1064 nmlaser, which by means of stabilization to a molecular iodine cell, reaches a frequency stability of approximately 1000 Hz/$\sqrt{\text{Hz}}$ at 1 mHz [22].

To generate the three frequencies needed in the experiment, the beam is split three ways and propagated through a double-pass acousto-optic modulators (AOMs) stage [23], enabling ∼MHz frequency shifts with high tuning bandwidths for fiber coupling. The Rx beam is further split by means of a half-wave plate and a polarizing beam splitter (PBS). The four resulting beams are coupled into single-mode polarization-maintaining optical fibers and delivered to TDOBS. The two Rx beams are directed to the Rx-GB fiber injector optical sub-assembly (FIOS) and to the flattop beam generator (Rx-FT) [18].

C. Photoreceivers

In this paper, we refer to the PR as the ensemble of PD and trans-impedance amplifier (TIA). LISA uses round quadrant photodiodes (QPDs), which are PDs with an active area which is split into four rotationally symmetric segments (see Fig. 2). Each QPD segment has a dedicated TIA.

Each quadrant photoreceiver (QPR) segment is required to have an electronic noise (expressed as input-equivalent current noise density) $\tilde{i}_{\text{en}}(f) < 2\ \text{pA}/\sqrt{\text{Hz}}$ in the LISA heterodyne band. An expression for $\tilde{i}_{\text{en}}(f)$ valid for beat note frequencies in the LISA heterodyne band is given in Eq. (1) [24]. Note that it is frequency dependent,

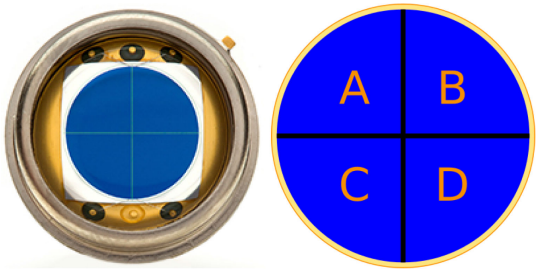

FIG. 2. Left: Picture of a QPD. Right: definition of the used segment-nomenclature throughout the paper. The area between the segments is called *slit*. Depending on the specific QPD model, the slit can be either insensitive, partially sensitive, or even more sensitive than the active area itself.

$$\tilde{i}_{\text{en}}(f) \approx \sqrt{\frac{4k_B T}{R_{\text{F}}} + \tilde{i}_{\text{ACE}}^2 + (2\pi f(C_{\text{PD}} + C_{\text{ACE}})\tilde{e}_{\text{ACE}})^2}. \quad (1)$$

In Eq. (1), the subscript ACE denotes the active circuit element used as an amplifier; $\tilde{i}_{\text{ACE}}$, $\tilde{e}_{\text{ACE}}$ and C_{ACE} represent its current noise density, voltage noise density and capacity, respectively. C_{PD} is the PD (or QPD segment)'s capacitance, R_{F} is the feedback resistance of the TIA and T is the temperature of the TIA, and k_B is the Boltzmann constant.

Reducing the electronic noise requires a careful design of the TIA and of the QPDs. In particular, the capacitance of each segment of the QPD has to be kept as low as possible; as $C_{\text{PD}} \propto r_{\text{QPD}}^2$ (r_{QPD} is the QPD's radius). This imposes an upper limit to the size of the QPD, introducing a trade-off with optimizing the DWS gain, which also scales with the QPD radius, as discussed in Sec. III.

The QPRs for TDOBS have been developed close to the current baseline, which is going to be build by Nikhef and SRON [25]. For the QPDs in TDOBS, the GAP1000Q model from OptoElectronics Components was chosen; these QPDs feature a 1 mm diameter and 20 μm sensitive slits. The TIAs are based on the current baseline for LISA and feature a transistor first-stage amplifier [25]. These TIAs have been characterized with the white-light method [24] and have an input equivalent current noise below 2 pA/$\sqrt{\text{Hz}}$ below the frequency of 15 MHz (see Fig. 3).

TDOBS employs a total of four such QPDs. Two serve as REFQPDs, placed on the TS in optical copies of the Rx-clip. The remaining two are SCIQPDs, positioned at the output port of the interferometer on the OB.

D. Imaging systems

Pupil-to-pupil imaging systems transfer both the spatial and angular properties of rays from a point in the entrance pupil plane to a conjugate point in the exit pupil plane, along the beam's propagation axis. Such systems, which consist of a combination of one or more lenses or curved

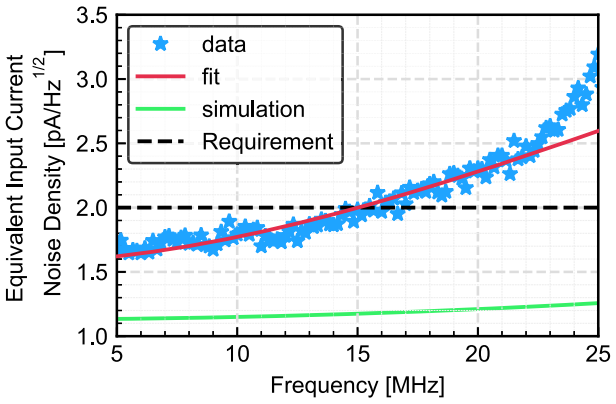

FIG. 3. Measurement, SPICE simulation, and fit of the electronic noise from the TIA used for the photodiodes in TDOBS. The fit function is $f(x) = \sqrt{p_0^2 + (p_1 x)^2}$, reproducing Eq. (1).

mirrors, can be used to mitigate the geometrical component of TTL [18] as well as beam walk, defined as the lateral displacement of the beam spot on the PD surface along one or both transverse axes as a function of the beam tilt. Mathematically, they can be described using the ray-transfer matrix formalism [26][Chap. 15] by a 2×2 $\left(\begin{smallmatrix} A & C \\ B & D \end{smallmatrix}\right)$ matrix with null B element. As ray-transfer matrices have a unitary determinant, this also implies that $D = A^{-1}$,

$$\mathbf{r}' = M_{\mathrm{IS}}\mathbf{r}, \qquad M_{\mathrm{IS}} = \begin{pmatrix} m^{-1} & 0 \\ C & m \end{pmatrix}, \tag{2}$$

where m is the *angular magnification* of the imaging system. Moreover, such systems can be designed to produce a collimated output for a collimated input by imposing $C = 0$ in Eq. (2). The imaging systems used in TDOBS and in LISA (including the telescope) are *collimating* imaging systems.

When a Gaussian beam is propagated through an imaging system, its mode parameters change. A property of collimating imaging systems is that, if a Gaussian beam with spot radius w_{in} and RoC R_{in} at the input pupil plane is propagated through the imaging system, the output beam has a spot radius and RoC of

$$w_{\mathrm{out}} = m^{-1} w_{\mathrm{in}} \tag{3}$$

$$R_{\mathrm{out}} = m^{-2} R_{\mathrm{in}}. \tag{4}$$

Imaging systems in LISA also serve to compress the beams, adapting their size to match the dimensions of the QPR. In particular, selecting $m > 1$ results in a reduced beam spot radius. As described by Eq. (2), the beam's incidence angle is magnified by a factor m when propagating through a collimating imaging system.

As depicted in Fig. 4, LISA is implementing these imaging systems such that the tilt pivot of the beam impinging on the PR coincides with the center of the PR itself. In LISA, the telescope acts as a four-mirror *collimating* imaging system that images the Rx beam onto the Rx-clip. Four-lens *collimating* imaging systems are placed in front of each QPR to further image the Rx-clip pupil plane onto the surface of the detector. Therefore, the description of tilts in LISA can be simplified to just tilts around the center of the QPDs.

E. Phasemeters

The phasemeter is the device tasked with reading out the phases of the electric beat notes from the QPR. TDOBS employs two phasemeters, both sampling at $f_s = 80$ MHz. The first one is based on I/Q demodulation and requires precise knowledge of the beat note frequencies to track. It is an old 16-channel model, not designed to reach the LISA phase noise requirement, and remains essential to TDOBS because its control software operates the steering mirrors on the TS. The second phasemeter is a LISA phasemeter engineering model pre-developement. It is an 8-channel version featuring digital phase-locked loop (DPLL) beat note tracking and is designed to reach the LISA performance up to its Nyquist frequency. The main noise limitations of this instrument are thermally induced phase fluctuations and ADC jitter. The latter problem is mitigated by injecting an electrical pilot tone signal which is tracked across all channels, allowing for post-processing corrections [27–29].

F. Differential power sensing

Differential power sensing (DPS) is a technique that uses a QPD to measure the position of an impinging beam. This information is obtained by comparing the power impinging in each segment, more specifically calculating the dimensionless quantities $\mathrm{DPS_v}$ (vertical DPS) and $\mathrm{DPS_h}$ (horizontal DPS),

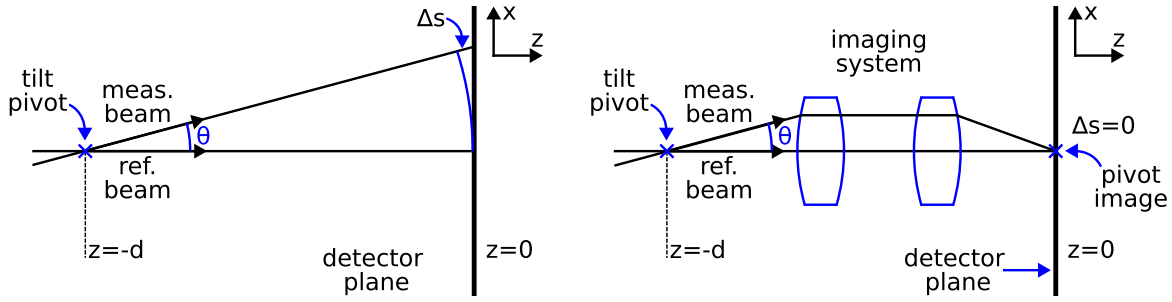

FIG. 4. Description of the lever arm effect between two beams. Two beams, the reference beam and the measurement beam, interfere. The resulting intensity is measured by a PR located on the $z = 0$ plane. The measurement beam can rotate about the pivot point $(0, 0, -d)^T$, representing either the Rx-clip or the TM's surface in LISA. Such a tilt causes the measurement beam to propagate through a longer path, with path length difference Δs. The extra path length is interferometrically measured at the PR; if Δs is not constant in time, it generates a noise floor. Such noise is called TTL. Imaging systems reduce the lever arm effect between two beams and beam walk by imaging the point of rotation of the beam into the center of the PR. This makes it such that the optical path length is unchanged by the tilt. As a consequence of this design, beam tilts in LISA have the center of the QPD as a pivot and reduced undesired beam walk on the QPD.

$$\mathrm{DPS_v} = \frac{P_{\mathrm{top}} - P_{\mathrm{bottom}}}{P_{\mathrm{top}} + P_{\mathrm{bottom}}} = \frac{P_A + P_B - P_C - P_D}{P_A + P_B + P_C + P_D} \quad (5)$$

$$\mathrm{DPS_h} = \frac{P_{\mathrm{left}} - P_{\mathrm{right}}}{P_{\mathrm{left}} + P_{\mathrm{right}}} = \frac{P_A - P_B + P_C - P_D}{P_A + P_B + P_C + P_D}. \quad (6)$$

The quantities $\mathrm{DPS_{v/h}}$ are related to the vertical/horizontal beam displacement from the center of the QPD, respectively. For a fundamental-mode Gaussian beam impinging on a QPD with zero slit width and infinite radius, the relation can be derived analytically [30] [Sec. 2.3.1],

$$\mathrm{DPS}(\Delta x) = -\mathrm{erf}\left(\frac{\sqrt{2}\Delta x}{w(z)}\right), \quad (7)$$

where $w(z)$ is the beam's spot radius at the QPD and Δx is the beam's displacement. Depending on the laser beam and QPD used, this technique can reach an alignment precision of the order of 1 μm. By using amplitude modulation techniques, it is possible to track the position of more than one beam on the same QPD. This is done in TDOBS for the Rx beam.

G. Differential wave front sensing

DWS [31,32] is a technique that uses a QPD to measure the angle between the wave fronts of two beams. The principle of the measurement is schematized in Fig. 5. A reference beam (red) and a measurement beam (blue) impinge on a QPD. The reference beam is assumed to be centered on the QPD and impinging orthogonally on it. The measurement beam is free to rotate around the center of the QPD as described in Fig. 4. The heterodyne interference of the two beams generates a beat note at each segment of the QPR. If the two beams are parallel, and neglecting small differences in the analog processing of these signals, all four beat notes share the same phase; however, phase offsets between the beat notes arise as soon as the measurement beam is tilted. These offsets can be recovered by comparing the phase readout of the segments, calculating the two quantities,

$$\mathrm{DWS_v} \coloneqq \phi_{\mathrm{top}} - \phi_{\mathrm{bottom}} = \frac{\phi_A + \phi_B - \phi_C - \phi_D}{2} \quad (8)$$

$$\mathrm{DWS_h} \coloneqq \phi_{\mathrm{left}} - \phi_{\mathrm{right}} = \frac{\phi_A - \phi_B + \phi_C - \phi_D}{2}, \quad (9)$$

where ϕ_i with $i \in (A, B, C, D)$ denotes the phase measured by QPD segment i (the segments of the QPDs follow the nomenclature in Fig. 5). $\mathrm{DWS_v}$ and $\mathrm{DWS_h}$ are functions of the vertical and horizontal beam tilts η and φ; therefore, by measuring these signals, it is possible to recover the relative wave front angle between the two beams.

The relation between the tilt angle and phase offset is approximately linear for small tilts. Let θ be the tilt angle; the proportionality coefficient between DWS and θ is κ_1. This parameter takes the name of *DWS* gain at zero angle. As later demonstrated in Sec. III, κ_1 is simply the first-order approximation of a more complicated function,

$$\mathrm{DWS} \approx \kappa_1 \theta, \qquad \kappa_1 \sim r_{\mathrm{QPD}}/\lambda \sim 10^3. \quad (10)$$

The second of Eq. (10) approximates the Gaussian beams to plane waves and plugs in typical numbers for LISA ($r_{\mathrm{QPD}} \sim 1$ mm, $\lambda = 1064$ nm). It must be pointed out that in LISA the two beams do not have the same frequency, as the interference is heterodyne. This frequency difference is of the order of 10^7 Hz; this value is small if compared to the frequency of the beam, which is of the order of 10^{14} Hz. Therefore, the difference in the wavelengths can also be neglected. A more detailed description requires considering the Gaussian nature of the beams in the calculation, as described in [33] in the case of a QPD much larger than the beams in size. A practical implementation of DWS in the phasemeter with some advantages is described in [34].

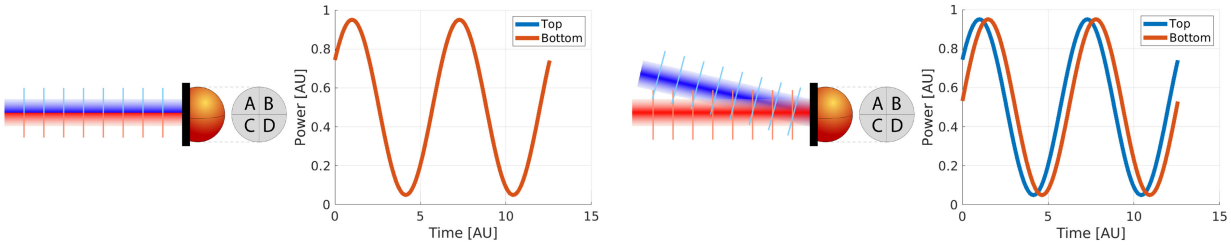

FIG. 5. Representation of a DWS measurement. Two Gaussian beams, a reference beam (red) and a measurement beam (blue), impinge on a QPD. The two beams have a frequency difference in the range of a few MHz and, therefore, generate a beat tone. Their wave fronts are, for simplicity, drawn as flat. Each segment of the QPD integrates the intensity impinging on it, resulting in a beat note at the heterodyne frequency. When the two beams are aligned, the beat notes from the four segments are in phase, as in the left figure. When a tilt occurs, as in the right figure, the wave fronts of the measurement beam reach the top segments earlier than the bottom segments. This causes a phase offset between the beat notes measured in the top and bottom segments. Such a phase offset is a function of the measurement beam's tilt angle.

H. Longitudinal path length signal

The use of a QPD also requires a definition of the overall phase signal of a QPD. This paper uses the average-phase LPS signal, defined as

$$\mathrm{LPS}_{\mathrm{AP}} = \frac{1}{k}\phi_{\mathrm{AP}} = \frac{1}{k}\frac{\phi_A + \phi_B + \phi_C + \phi_D}{4}, \tag{11}$$

where $k = \frac{2\pi}{\lambda}$ is the wave number.

III. DWS SIGNAL MODEL

This section derives the relation between the DWS signals in Eqs. (8) and (9) and the tilt angle θ in the case of the interference of two fundamental-mode Gaussian beams being detected by a QPD. This estimation can be done analytically under the assumption that the QPD's radius is much larger than the beam's spot radius; this is calculated in Sec. III A. An analytical extension of this method to a finite and circular QPD is possible if the wave front curvature mismatch is small; this is calculated in Sec. III B. A numerical model is required if these conditions are not satisfied. We report one such model in Sec. III C, which we compare against the analytical expressions.

A. DWS analytical model for an infinite QPD

This calculation starts as in [33] in the case of a rotation around the QPD's center and leads to the same result. A depiction of the framework is shown in Fig. 6. Two fundamental-mode Gaussian beams are assumed. Let $\vec{x} = (x, y, z)^T$ be the coordinates of laboratory's reference frame (RF). In this RF, the QPD is a surface defined by $z = 0$, and the reference beam propagates along the z-axis. The electric field of the reference beam in the lab's RF is

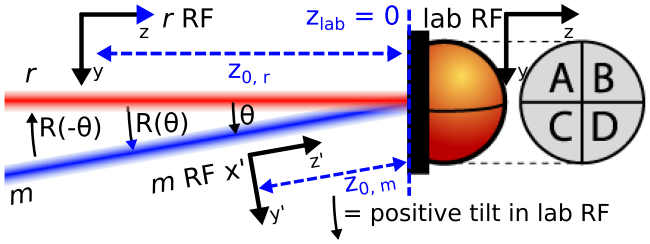

FIG. 6. Framework of the used reference frames. The QPD defines the lab's RF, with the QPD's center being located at $\vec{x} = \vec{0}$. The reference beam's RF shares the same coordinates with the lab's RF but is shifted along the z-axis. The measurement beam's RF is rotated and shifted along the z-axis with respect to the lab's RF. A positive tilt of the beam is defined as an anticlockwise tilt. The measurement beam's RF can be obtained by rotating the lab's RF by an angle $-\theta$. Dually, the lab's RF can be obtained by rotating the measurement beam's RF by an angle θ. The tilt shown in the figure causes the measurement beam's path length to the top segments A and B to be larger than that to the bottom segments C and D. Therefore, in such a configuration, the DWS signal is positive.

$$\vec{E}(\vec{x})_r = \mathrm{Re}[E_r \hat{\epsilon}_r \mathcal{E}_r(\vec{x})], \tag{12}$$

where $E_r \in \mathbb{C}$ [V/m] is the beam's amplitude and $\hat{\epsilon}_r = (\epsilon_{x,r}, \epsilon_{y,r}, 0)^T$, $\epsilon_{x,r}, \epsilon_{y,r} \in \mathbb{C}$, $\hat{\epsilon}_r \perp \hat{\epsilon}_z$ is a generic polarization unitary vector of an electromagnetic wave propagating along the z-axis and $\mathcal{E}_r(\vec{x})$ is the complex scalar wave amplitude,

$$\mathcal{E}_r(\vec{x}) = \sqrt{\frac{2}{\pi}}\frac{w_{0,r}}{w_r(z_r)}\exp\left(-\frac{x^2+y^2}{w_r(z_r)^2} + i\left(k\frac{x^2+y^2}{2R_r(z_r)} + kz_r + \eta(z_r)\right)\right), \tag{13}$$

where $z_r = z - z_{0,r}$ is the waist position adjusted z-coordinate and $w_{0,r}$ is the reference beam's waist, $w_r(z_r)$, $R_r(z_r)$ and $\eta(z_r)$ are the reference beam's spot radius, RoC and Guoy phase at the position z_r, respectively, defined as

$$w_r(z_r) = w_{0,r}\sqrt{1 + \left(\frac{z_r}{z_{R,r}}\right)^2}, \tag{14}$$

$$R_r(z_r) = z_r\left(1 + \left(\frac{z_{R,r}}{z_r}\right)^2\right), \tag{15}$$

$$\eta(z_r) = \arctan\left(\frac{z_r}{z_{R,r}}\right), \tag{16}$$

where $z_{R,r} = \pi w_{0,r}^2 \lambda^{-1}$ is the *Rayleigh range* of the reference beam. For typical LISA-parameters, $w_{0,r} \sim 1$ mm and $z_{R,r} \sim 10^3$ mm. From here on, the evaluation of these functions at z_r will be mostly implicit. Equation (13) is normalized such that

$$\int_{\mathbb{R}^2} |\mathcal{E}_r(\vec{x})|^2 \, \mathrm{d}x \, \mathrm{d}y = w_{0,r}^2, \ \forall \ z. \tag{17}$$

The measurement beam propagates on a generic axis, which is rotated by a small angle θ around the QPD's center with respect to the z-axis called z'. This axis is used to define the measurement beam's RF, which uses the primed coordinates $\vec{x}' = (x', y', z')^T$. Without loss of generality, this rotation is assumed to be a pitch (vertical) rotation. As justified in Fig. 4, the rotation pivot can be assumed to be the QPD's center $(x, y, z)^T = (0, 0, 0)^T$. Therefore, the lab's RF and measurement beam's RF are related by a rotation matrix,

$$\begin{pmatrix} x \\ y \\ z \end{pmatrix} = \begin{pmatrix} 1 & 0 & 0 \\ 0 & \cos(\theta) & \sin(\theta) \\ 0 & -\sin(\theta) & \cos(\theta) \end{pmatrix} \begin{pmatrix} x' \\ y' \\ z' \end{pmatrix} \quad \text{or} \quad \vec{x} = R(-\theta)\vec{x}'. \tag{18}$$

The electric field of the measurement beam is expressed by the same Eqs. (19) and (13) in the measurement beam's RF. We name this quantity,

$$\vec{E}'_m(\vec{x}') = \mathrm{Re}[E'_m \hat{\varepsilon}'_m \mathcal{E}'_m(\vec{x}')]. \tag{19}$$

Expressing it in the lab's RF requires a change of coordinates. The electric field is a vector field and transforms as

$$\vec{E}(\vec{x}) = R(-\theta)\vec{E}'(\vec{x}') = R(-\theta)\vec{E}'(R(\theta)\vec{x}), \tag{20}$$

where in the second step Eq. (18) has been used. The resulting electric field can be expressed again in the form,

$$\vec{E}_m(\vec{x},\theta) = \mathrm{Re}[E_m \hat{\varepsilon}_m(\theta)\mathcal{E}_m(\vec{x},\theta)], \tag{21}$$

where the dependency on θ has been added. We now evaluate the relation between all primed and unprimed quantities. The beam's amplitude E'_m is a scalar and does not vary in the change of coordinates: $E_m = E'_m$. The scalar wave amplitude $\mathcal{E}_{m,\mathrm{full}}(\vec{x},\theta)$ can be obtained by changing coordinates to its argument according to Eq. (20),

$$\begin{aligned}\mathcal{E}_{m,\mathrm{full}}(\vec{x},\theta) &= \mathcal{E}'_m(R(\theta)\vec{x}) \\ &= \sqrt{\frac{2}{\pi}}\frac{w_{m,0}}{w_m(\sin(\theta)y+z_m)}\exp\left(-\frac{x^2+(\cos(\theta)y+\sin(\theta)z)^2}{w_m(\sin(\theta)y+z_m)^2}\right. \\ &\quad \left. +i\left(k\frac{x^2+(\cos(\theta)y+\sin(\theta)z)^2}{2R_m(\sin(\theta)y+z_m)}+k(\sin(\theta)y+z_m)+\eta(\sin(\theta)y+z_m)\right)\right),\end{aligned} \tag{22}$$

where $z_m = \cos(\theta)(z - z_{0,m})$ is the waist position adjusted z-coordinate in the lab's RF. Note that, according to Eq. (20), the polarization unitary vector is also rotated by $R(-\theta)$ and becomes

$$\hat{\varepsilon}'_m = \begin{pmatrix}\epsilon_{x,m}\\ \epsilon_{y,m}\\ 0\end{pmatrix} \rightarrow \hat{\varepsilon}_m(\theta) = R(-\theta)\hat{\varepsilon}'_m = \begin{pmatrix}\epsilon_{x,m}\\ \cos(\theta)\epsilon_{y,m}\\ \sin(\theta)\epsilon_{y,m}\end{pmatrix}. \tag{23}$$

The tilt introduces a dependence of the beam spot radius $w_m(z_m)$, RoC $R_m(z_m)$, and Guoy phase $\eta(z_m)$ on the transverse coordinate y. As the tilts are small $\theta \lessapprox 1$ mard, we can assess the significance of this dependency with a Maclaurin expansion, shown in Eqs. (24)–(26),

$$w_m(\cos(\theta)z_m+\sin(\theta)) \approx w_m(z_m)\left(1+\frac{z_m\theta y}{z_{R,m}^2+z_m^2}\right)+O(\theta)^2 = w_m(z_m)(1+10^{-6}), \tag{24}$$

$$R_m(\cos(\theta)z_m+\sin(\theta)) \approx R_m(z_m)(1+\theta y)+O(\theta)^2 = R_m(z_m)(1+10^{-3}), \tag{25}$$

$$\eta(\cos(\theta)z_m+\sin(\theta)) \approx \eta(z_m)\left(1+\frac{1}{\eta(z_m)}\frac{z_{R,m}^2}{z_{R,m}^2+z_m^2}\frac{y\theta}{z_{R,m}}\right)+O(\theta)^2 = \eta(z_m)(1+10^{-6}). \tag{26}$$

The resulting first-order terms in θ are negligible in all three cases. This can be seen by substituting typical system parameters: $\theta \lessapprox 1$ mrad, $y \sim 1$ mm (as the value of y is limited by either the PD's size or the beam's size), and that the distance between the beam's waist position and the PD's position is within the beam's Rayleigh range, $z_m \lessapprox z_{R,m} \sim 10^3$ mm.

Also note that the use of first-order expansions for Eqs. (24) and (25) would lead to third-order terms in y in the exponential. As $\int_{-\infty}^{+\infty}\exp(y^3)dy$ can not be integrated, we are forced to use the zero-order approximation for $w_m(z_m)$ and $R_m(z_m)$. Expanding the term $\eta(z_m)$ to first-order in y would not harm the integrability of the resulting intensity, but we chose to fix the same order of approximation in y for all three terms $w_m(z_m)$, $R_m(z_m)$, $\eta(z_m)$. We therefore approximate the beam's spot size, RoC, and Gouy phase to zero-order in θ. We later show that such an approximation still describes extremely well the DWS signal.

The path length term $\exp(ik\theta y)$, however, cannot be neglected, as it significantly changes the phase of the beam

along the y-axis. This is because the product $ky\theta = 2\pi\theta y/\lambda$ is of order unity. A first-order Maclaurin expansion of this term would require $\theta y/\lambda \ll 1$, corresponding to $\theta \lessapprox 10^{-4}$ rad at LISA's wavelength of 1064 nm. Such an expansion is reasonable only for analyzing extremely small tilts of the order of a few μrad.

With this knowledge, the quantity $\mathcal{E}_{m,\mathrm{full}}(\vec{x},\theta)$ in Eq. (22) can be simplified into

$$\mathcal{E}_{m,\mathrm{approx}}(\vec{x},\theta) = \sqrt{\frac{2}{\pi}}\frac{w_{m,0}}{w_m}\exp\left(-\frac{x^2+y^2}{w_m^2} + i\left(k\frac{x^2+y^2}{2R_m} + \underbrace{ky\theta}_{\text{tilt}} + kz_m + \eta(z_m)\right)\right). \tag{27}$$

From now onward, the simplified expression in Eq. (27) is going to be used. The intensity of the superimposed reference and measurement beams is

$$\begin{aligned} I_{\mathrm{ifm}}(x,y,\theta) &= \frac{1}{2Z}[|\vec{E}_r + \vec{E}_m|^2] \\ &= \frac{1}{2Z}[|\vec{E}_r|^2 + |\vec{E}_m|^2 + \vec{E}_r\cdot\vec{E}_m^* + \vec{E}_r^*\cdot\vec{E}_m], \end{aligned} \tag{28}$$

where $\cdot^*$ indicates complex conjugation and $Z[\Omega]$ is the wave impedance of the medium in which the beam is propagating.

Substituting the explicit expressions for the reference and measurement beams from Eqs. (13) and (27) in Eq. (28) yields the full expression for the overlapped reference and measurement beams' intensity,

$$\begin{aligned} I_{\mathrm{ifm}}(x,y,\theta) = \frac{1}{Z\pi}\Bigg[&\underbrace{\left(E_r\frac{w_{r,0}}{w_r}\right)^2\exp\left(-2\frac{x^2+y^2}{w_r^2}\right)}_{|\vec{E}_r|^2} + \underbrace{\left(E_m\frac{w_{m,0}}{w_m}\right)^2\exp\left(-2\frac{x^2+y^2}{w_m^2}\right)}_{|\vec{E}_m|^2} \\ &\underbrace{+\hat{\varepsilon}_r\cdot\hat{\varepsilon}_m\left(E_r\frac{w_{r,0}}{w_r}E_m\frac{w_{m,0}}{w_m}\exp\left(-2\frac{x^2+y^2}{w_{\mathrm{eff}}^2}(1-i\rho) + i(kz_r+\eta(z_r)-ky\theta-kz_m-\eta(z_m))\right) + \mathrm{c.c.}\right)}_{\vec{E}_r\cdot\vec{E}_m^*+\vec{E}_r^*\cdot\vec{E}_m}\Bigg], \end{aligned} \tag{29}$$

where the quantities,

$$\frac{2}{w_{\mathrm{eff}}^2} = \frac{1}{w_r^2(z_r)} + \frac{1}{w_m^2(z_m)}, \tag{30}$$

$$\frac{1}{R_{\mathrm{rel}}} = \frac{1}{R_r(z_r)} - \frac{1}{R_m(z_m)}, \tag{31}$$

$$\rho = \frac{w_{\mathrm{eff}}^2 k}{4R_{\mathrm{rel}}}, \tag{32}$$

have been introduced. The quantity w_{eff} is the effective spot radius of the two overlapped beams, and R_{rel} is their absolute wave front curvature mismatch. The quantity ρ is the effective-spot-radius-normalized wave front curvature mismatch. As both R_{rel} and ρ—and also θ—are odd under the swapping of the two beams, any physical effect of a combination of these parameters must respect this symmetry. The parameter ρ is a function of both beams' parameters. By substituting Eqs. (14) and (15) into Eqs. (30) and (31), and then into Eq. (32), one can derive an expression for ρ that depends only on the fundamental parameters of the two interfering Gaussian beams,

$$\rho = \frac{\pi^2\lambda(w_{m,0}^4 z_r - w_{r,0}^4 z_m) + \lambda^3 z_r z_m(z_m - z_r)}{\pi\lambda^2(w_{r,0}^2 z_m^2 + w_{m,0}^2 z_r^2) + \pi^3 w_{r,0}^2 w_{m,0}^2(w_{r,0}^2 + w_{m,0}^2)}. \tag{33}$$

Although the value of ρ can become significant under certain conditions, such as large values of $z_{r,m}$ combined with small waist radii, typically it is smaller than 1.

Our goal is to derive the phase variation measured by a PD due to the tilt, which is defined as the argument of the integral of the overlap term $\frac{1}{Z\pi}\vec{E}_r(\vec{x})\cdot\vec{E}_m^*(\vec{x},\theta)$ over the PD's surface [18],

$$\varphi_{\mathrm{PD}} = \arg(P_{\mathrm{PD}}) = \arg\left(\int_{S_{\mathrm{PD}}}\frac{1}{Z\pi}\vec{E}_r(x,y)\cdot\vec{E}_m^*(x,y,\theta)\mathrm{d}S\right). \tag{34}$$

For calculating the phase variation, multiplicative factors such as $\frac{1}{Z\pi}E_r\frac{w_{r,0}}{w_r}E_m\frac{w_{m,0}}{w_m}$ and constant phase terms like

$\exp(+kz_r + \eta(z_r) - kz_m - \eta(z_m))$ can be dropped as they do not contribute to the final DWS signal.

From here on, we assume that both beams have linear, horizontal polarization. Since the tilt is vertical, this results in $\hat{\varepsilon}_r \cdot \hat{\varepsilon}_m = 1$, independent of θ. Note that if both polarization and tilt were vertical, then the scalar product $\hat{\varepsilon}_r \cdot \hat{\varepsilon}_m = \cos(\theta)$ would depend on the tilt angle. This effect, although negligible, must be taken into account due to the vector nature of the electric field. A simplified interference term for integration over the PD area is therefore defined as

$$I_{\mathrm{smp}}(x, y, \theta) = \exp\left(-2\frac{x^2 + y^2}{w_{\mathrm{eff}}^2}(1 - i\rho) - iky\theta\right) + \mathrm{c.c.} \tag{35}$$

Equation (35) is to be understood as a distribution of local phase offsets, given by the imaginary part of the equation, multiplied by the local intensity of the beam overlap, given by the real part of the equation. To derive the DWS signals, Eq. (35) must be integrated over the surface of the QPD to obtain the optical power incident on each QPD segment. This procedure *de facto* performs the amplitude-weighted sum of the phase offsets at each point of the QPD's surface. This integration can be performed analytically only under the assumption that the QPD radius r_{QPD} is much larger than the effective beam spot radius w_{eff}, allowing the integration limits to be extended to infinity. As a further simplification, the slit width is neglected. Taking the argument of the resulting complex integral yields the phase of the beat note on each segment. Exploiting the property of the argument function $\arg(z_1) + \arg(z_2) = \arg(z_1 z_2)$ simplifies the derivation, leading to the following expression for the DWS signals:

$$\mathrm{DWS_v}(\theta) = \arg\left(\frac{\int_{-\infty}^{+\infty} \mathrm{d}x \int_{0}^{+\infty} \mathrm{d}y I_{\mathrm{smp}}(x, y, \theta)}{\int_{-\infty}^{+\infty} \mathrm{d}x \int_{-\infty}^{0} \mathrm{d}y I_{\mathrm{smp}}(x, y, \theta)}\right) \tag{36}$$

$$\mathrm{DWS_h}(\theta) = \arg\left(\frac{\int_{-\infty}^{0} \mathrm{d}x \int_{-\infty}^{+\infty} \mathrm{d}y I_{\mathrm{smp}}(x, y, \theta)}{\int_{0}^{+\infty} \mathrm{d}x \int_{-\infty}^{+\infty} \mathrm{d}y I_{\mathrm{smp}}(x, y, \theta)}\right). \tag{37}$$

By solving the integrals in Eqs. (36) and (37), one gets

$$\mathrm{DWS_v}(\theta) = \arg\left(\frac{1 - i\alpha}{1 + i\alpha}\right), \qquad \mathrm{DWS_h}(\theta) = 0, \tag{38}$$

with

$$\alpha = \mathrm{erfi}\left(\frac{kw_{\mathrm{eff}}\theta}{2^{\frac{3}{2}}\sqrt{1 - i\rho}}\right) = \mathrm{erfi}\left(\frac{kw_{\mathrm{eff}}\theta}{2^{\frac{3}{2}}} \frac{e^{\frac{i}{2}\arctan\rho}}{\sqrt[4]{1 + \rho^2}}\right), \tag{39}$$

and where $\mathrm{erf}(iz) = i\mathrm{erfi}(z)$ is the *imaginary error function*. As to be expected, $\mathrm{DWS_h}(\theta) = 0$ for symmetry reasons and $\mathrm{DWS_v}(\theta)$ is an odd function of θ. As $\mathrm{erfi}(z^*) = \mathrm{erfi}^*(z)$, Eqs. (38) and (39) do not depend on the sign of ρ, hence respecting the previously mentioned symmetry of the system under beam-swap.

According to how the angles and the DWS signals are defined in Eqs. (8) and (9), note that there is a sign difference between a vertical and horizontal tilt, as in the case of a solely horizontal tilt the DWS signals are

$$\mathrm{DWS_v}(\theta) = 0, \qquad \mathrm{DWS_h}(\theta) = \arg\left(\frac{1 + i\alpha}{1 - i\alpha}\right). \tag{40}$$

This last case is taken from here onwards. Note that Eqs. (38) and (39) depend on θ, w_{eff} and k only through their product $\Theta = kw_{\mathrm{eff}}\theta$, meaning that the result for specific values of k and w_{eff} can be carried over to different values simply by an appropriate rescaling of the angle θ. An example of the DWS signal on an infinite QPD is shown in Fig. 7.

Since we are interested mostly in situations where θ is very small, it is reasonable to expand the expressions in Eqs. (38) and (39) around $\theta = 0$. To do so, it is first convenient to split the argument of the imaginary error function in Eq. (39) into its real and imaginary parts,

$$\mathrm{Re}\left[\frac{kw_{\mathrm{eff}}\theta}{2^{\frac{3}{2}}\sqrt{1 - i\rho}}\right] = \frac{kw_{\mathrm{eff}}\theta}{2^{\frac{3}{2}}} F(\rho) \tag{41}$$

$$\mathrm{Im}\left[\frac{kw_{\mathrm{eff}}\theta}{2^{\frac{3}{2}}\sqrt{1 - i\rho}}\right] = \frac{kw_{\mathrm{eff}}\theta}{2^{\frac{3}{2}}} G(\rho) \tag{42}$$

with

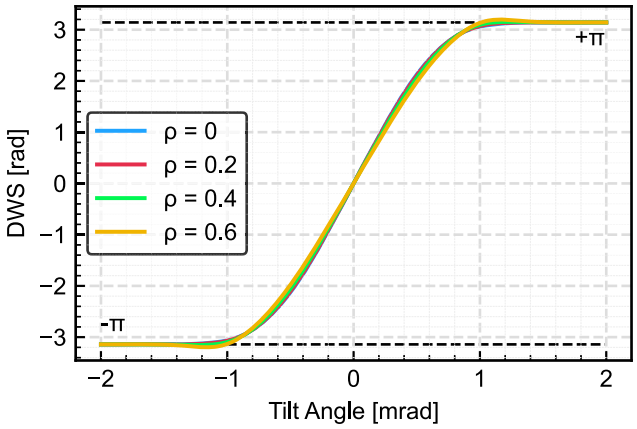

FIG. 7. Plot of the DWS signal on an infinite QPD in Eqs. (40) and (39) for $w_{\mathrm{eff}} = 1$ mm and for four specific values of ρ. Note that the DWS signal saturates to the asymptotic values $\pm\pi$ for large tilts $\theta \to \pm\infty$. The range of the DWS signal is proportional to the inverse of the used w_{eff}. For tilts around 1 mrad in this figure, the DWS signal reverses sign due to the fringe crossing. This sign reversal takes place only if $\rho \neq 0$ and is visible in the plot when the plots where the DWS signal crosses the $\pm\pi$ lines. In this plot, the DWS signal was unwrapped for plotting clarity.

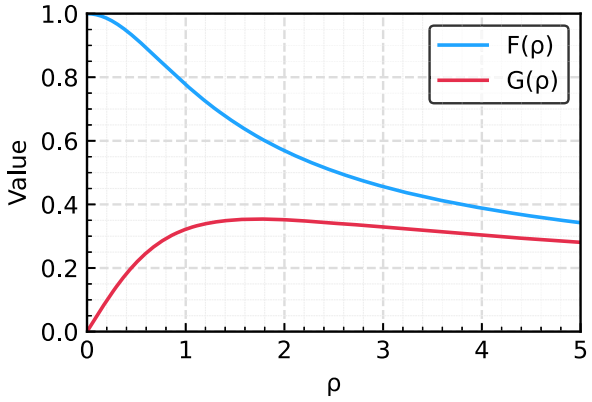

FIG. 8. Plot of the functions $F(\rho)$ and $G(\rho)$ in Eqs. (43) and (44) in the range $\rho \in [0, 5]$. The parameter ρ is the effective-spot-radius-normalized wave front mismatch. For typical values of ρ, $F(\rho)$ tends to one, while $G(\rho)$ tends to zero.

$$F(\rho) = (1+\rho^2)^{-\frac{1}{4}} \cos\left(\frac{1}{2}\arctan\rho\right) = \sqrt{\frac{1+\sqrt{1+\rho^2}}{2(1+\rho^2)}} \tag{43}$$

$$G(\rho) = (1+\rho^2)^{-\frac{1}{4}} \sin\left(\frac{1}{2}\arctan\rho\right) = \frac{\rho}{\sqrt{1+\rho^2}\sqrt{2(1+\sqrt{1+\rho^2})}}. \tag{44}$$

Note that $F(\rho)$ is an even function of ρ, while $G(\rho)$ is odd. Furthermore, since ρ assumes small values in this context, it is reasonable to also expand Eqs. (43) and (44) around $\rho = 0$, yielding

$$F(\rho) = 1 - \frac{3}{8}\rho^2 + \mathcal{O}(\rho^4) \tag{45}$$

$$G(\rho) = \frac{1}{2}\rho + \mathcal{O}(\rho^3). \tag{46}$$

Equation (45) is reported also in [33]. The functions $F(\rho)$ and $G(\rho)$ are plotted in Fig. 8.

The first three nonzero terms of the Maclaurin expansion of $\mathrm{DWS_v}(\theta)$ for an infinite QPD in Eq. (38) are reported in Eqs. (47)–(50),

$$\mathrm{DWS_v}(\theta) = \kappa_{1,\infty}\theta + \kappa_{3,\infty}\theta^3 + \kappa_{5,\infty}\theta^5 + \mathcal{O}(\theta^7) \tag{47}$$

$$\kappa_{1,\infty} = \sqrt{\frac{2}{\pi}}(kw_{\mathrm{eff}})F(\rho) \tag{48}$$

$$\kappa_{3,\infty} = -\frac{(kw_{\mathrm{eff}})^3}{6(2\pi)^{\frac{3}{2}}}(F(\rho)(F(\rho)^2 - 3G(\rho)^2)(4-\pi)) \tag{49}$$

$$\kappa_{5,\infty} = -\frac{(kw_{\mathrm{eff}})^5}{240(2\pi)^{\frac{5}{2}}}F(\rho)(F(\rho)^4 - 10F(\rho)^2G(\rho)^2 + 5G(\rho)^4)(\pi(40-3\pi) - 96). \tag{50}$$

Note that κ_3 and κ_5 are always negative, so that the DWS gain decreases as θ departs from zero. The corresponding orders of magnitude with LISA-like beam parameters are $\kappa_1 \sim 10^3$ rad/rad, $\kappa_3 \sim 10^9$ rad/rad^3 and $\kappa_5 \sim 10^{13}$ rad/rad^5 It can now be readily seen that the DWS signal is not linear, as in the approximation (10), and its shape depends on the interfering beams' waist and RoC.

B. DWS model for a finite QPD

We now derive the first-order Maclaurin expansion coefficient κ_1 for the case of a finite QPD with no slits. The term $\exp(ik\theta y)$ in Eq. (27) which prevents analytical integration on a finite PD, is expanded to first order to derive the linear DWS gain coefficient $\kappa_{1,\circ}$ for a generic QPD radius, and to third order to derive $\kappa_{3,\circ}$. While this approximation might seem to further limit the angular validity range, this effect is counteracted by the finite size of the QPD. We argued in Sec. III A that no expansion of $\exp(ik\theta y)$ is possible for an infinite detector because the product $k\theta y$ can be of order one, where y is determined by the beam size ($y \sim 1$ mm). For a finite QPD, however, the integration is limited by the detector radius r_{QPD}, so the relevant scale is $y \sim r_{\mathrm{QPD}}$. In this context, the condition $k\theta y \ll 1$ can hold for larger angles. For $r_{\mathrm{QPD}} = 0.1$ mm, this expansion is expected to be valid for angles up to $\theta \lessapprox 1$ mrad. With this approximation, the intensity in Eq. (35) becomes Eq. (52), which can be integrated analytically over a finite circular area of radius r_{QPD} in polar coordinates (r, ψ). The integration over the top half of the QPD in Eq. (51) gives the power $P_{\mathrm{top}}(\theta)$,

$$P_{\mathrm{top}}(\theta) = \int_0^{\pi} \mathrm{d}\psi \int_0^{r_{\mathrm{QPD}}} I_{\mathrm{smp\text{-}1st}} r \mathrm{d}r = \frac{w_{\mathrm{eff}}^2}{4(1-i\rho)^{3/2}}\left(\sqrt{1-i\rho}\left(\pi - e^{-2\frac{r_{\mathrm{QPD}}^2}{w_{\mathrm{eff}}^2}(1-i\rho)}(\pi + i2kr_{\mathrm{QPD}}\theta)\right) + kw_{\mathrm{eff}}\sqrt{\frac{\pi}{2}}\mathrm{erfi}\left(i\frac{\sqrt{2}r_{\mathrm{QPD}}}{w_{\mathrm{eff}}}\sqrt{1-i\rho}\right)\right) + \mathrm{c.c.}, \tag{51}$$

where

$$I_{\text{smp-1st}}(x,y,\theta) = \exp\left(-2\frac{x^2+y^2}{w_{\text{eff}}^2}(1-i\rho)\right)(1-iky\theta+\mathcal{O}(k\theta y)^2)+\text{c.c.} \tag{52}$$

Similarly, $P_{\text{bottom}}(\theta) = P_{\text{top}}(-\theta)$. Extracting the phase from Eq. (51) can be done by calculating its argument, omitting the complex conjugate term. However, this operation is analytically intractable because the imaginary error function cannot be separated into real and imaginary parts in closed form. This term depends on the ρ parameter, which quantifies the mismatch between the two spherical wave fronts tilting around a common pivot, namely the center of the QPD. As previously discussed, the DWS signal is independent on the sign of ρ, implying that ρ can appear only in second-order terms of a Taylor expansion. Given that typically $\rho < 1$, it is reasonable to neglect it to first order and set $\rho = 0$. Under this assumption, one obtains the value of $\kappa_{1,\circ}$ for a finite and slitless QPD in Eq. (53). For notation simplicity, the quantity $\beta = \sqrt{2}r_{\text{QPD}}/w_{\text{eff}}$ was introduced,

$$\kappa_{1,\circ,\rho-0} = \frac{\sqrt{2}kw_{\text{eff}}(\sqrt{\pi}\text{erf}(\beta)-2\beta e^{-\beta^2})}{\pi(1-e^{-\beta^2})}. \tag{53}$$

In the limit for large QPD radius, the previous expression for $\kappa_{1,\infty}$ evaluated at $\rho = 0$ is recovered,

$$\lim_{\beta\to\infty}\kappa_{1,\circ,\rho-0} = \kappa_{1,\infty}(\rho=0). \tag{54}$$

As expected, the newly obtained information confirms that

$$\lim_{\beta\to 0}\kappa_{1,\circ,\rho-0} = 0. \tag{55}$$

To include the effect of the wave front mismatch, one can perform a second-order Maclaurin expansion of Eq. (51) in the ρ parameter. This requires expanding all ρ-dependent terms, including the imaginary error function, erfi$(\cdot)$, to second order,

$$\text{erfi}(ia\sqrt{1-i\rho}) \approx i\text{erf}(a) - \frac{ae^{-a^2}}{\sqrt{\pi}}\rho + i\frac{a(2a^2+1)e^{-a^2}}{4\sqrt{\pi}}\rho^2. \tag{56}$$

This calculation results in a correction term that captures the leading-order contribution of the wave front mismatch to the detected signal. Note that the linear terms in ρ in Eq. (56) cancel out in the estimation of the κ coefficients. To fourth-order in ρ, the linear DWS gain coefficient is

$$\kappa_{1,\circ} = \kappa_{1,\circ,\rho-0} + \kappa_{1,\circ,\rho-2}\rho^2 + \mathcal{O}(\rho^4). \tag{57}$$

We report the expression of $\kappa_{1,\circ,\rho-2}$ in Eq. (A1). One can see that in the limit of large QPD radius, the second order expansion of $\kappa_{1,\infty}$ in Eq. (48) around $\rho = 0$ is recovered. This is $\kappa_{1,\infty}$ times Eq. (45),

$$\lim_{\beta\to\infty}\kappa_{1,\circ,\rho} = k_{1,\infty}\left(1-\frac{3}{8}\rho^2\right). \tag{58}$$

A first-order expansion of the term $\exp(-ik\theta y)$ leads to an approximate expression for the first order DWS coefficient κ_1. A similar procedure can be followed to derive κ_3 by expanding the term $\exp(-ik\theta y)$ in Eq. (27) to third order in θ. The same analysis, albeit with much lengthier calculations, leads to an expression for $\kappa_{3,\circ}$ of the same kind as Eq. (57),

$$\kappa_{3,\circ} = \kappa_{3,\circ,\rho-0} + \kappa_{3,\circ,\rho-2}\rho^2 + \mathcal{O}(\rho^4). \tag{59}$$

The expressions for the quantities $\kappa_{3,\circ,\rho-0}$ and $\kappa_{3,\circ,\rho-2}$ are given in Eqs. (A2), (A3), respectively. As expected, the limit values of Eq. (59) are

$$\lim_{\beta\to 0}\kappa_{3,\circ} = 0 \tag{60}$$

$$\lim_{\beta\to\infty}\kappa_{3,\circ} = \kappa_{3,\infty}\left(1-\frac{15}{8}\rho^2\right). \tag{61}$$

C. DWS numerical model for a generic QPD

A numerical model can be developed to address all DWS signal calculations that cannot be carried out analytically. These include arbitrary QPD geometries and values of ρ that extend beyond the validity range of the previous Maclaurin expansions. The model is also used to verify the validity of the previous analytical approximations, as those performed between Eqs. (22) and (27). The power incident on each QPD segment is computed by numerically integrating the beam intensity [Eq. (35) in the approximated case], employing a discretization of both the QPD surface and the tilt angles. The corresponding phase is then extracted as the argument of the resulting complex power $P_{\text{num}}(\theta)$,

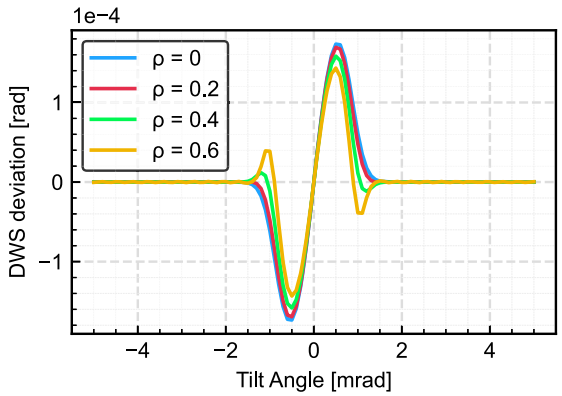

FIG. 9. Plot of the difference between numerically calculated DWS signal and the analytically calculated DWS signal for a $w_{\mathrm{eff}} = 1$ mm beam an infinite QPD. In both cases, the approximated expression for the intensity in Eq. (27) is used. This results in the numerical integration's artifacts; note that the magnitude of such artifact depends on the spatial discretization Δs^2 used in the numerical integration; the result plotted in this figure uses $\Delta s = 5$ μm.

$$P_{\mathrm{num}}(\theta) = \int\int_{S_{\mathrm{QPD}}} \mathrm{d}x\mathrm{d}y I_{\mathrm{smp}}(x,y,\theta) \approx \sum_{i}^{x_i \in S_{\mathrm{QPD}}} \sum_{j}^{y_j \in S_{\mathrm{QPD}}} I_{\mathrm{smp}}(x_i,y_j,\theta_k)\Delta s^2 + \mathcal{O}(\Delta s^4). \quad (62)$$

As the amount of sums to be taken is proportional to Δs^2, the discretization introduces an overall numerical error that scales as Δs^2. We found that a spatial resolution of $\Delta s = 5$ μm, which limits the integration's runtime to a few seconds, induces DWS numerical artifacts of approximately 100 μrad at most for a beam of effective spot radius 1 mm, which is well within the target precision of this model (see Fig. 9). From the numerically computed power $P_{\mathrm{num}}(\theta)$, the phase is extracted by evaluating its complex argument, and the corresponding DWS signal is subsequently derived from this phase. Finally, the parameters κ_1 and κ_3 are obtained by performing a linear fit of the resulting DWS signal. We stress that this process is sensitive to the used angular fitting range.

Numerical integrations are used to assess the validity of the approximations in Eqs. (24)–(26) introduced between Eqs. (22) and (27). The discrepancy between the fully numerically integrated DWS signal and the approximated numerically integrated DWS signal is of the order of 10^{-7} rad. Note that such deviation is smaller than that reported in Fig. 9; this is due to the fact that both numerical integrations introduce very close artifacts, which are canceling out in Fig. 10. We conclude that this analytical model can estimate the DWS signal with deviations smaller than 100 μrad. We argue that reducing this deviation estimation by decreasing Δs is computationally intensive and beyond the scope of this work.

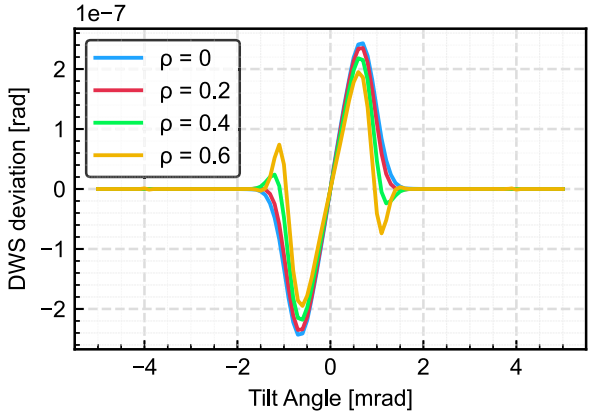

FIG. 10. Plot of the difference between numerically calculated full DWS signal and approximated DWS signal. The full DWS signal uses Eq. (22) for the electric field of the measurement beam, while the approximated DWS signal uses Eq. (27). The used beam parameters are $w_{\mathrm{eff}} = 1$ mm, and the QPD size is infinite. This numerical calculation shows that the two results are extremely close, with differences as little as 10^{-7} rad, with little dependence on the normalized wave front curvature mismatch parameter ρ.

Numerical integrations are also used to assess the validity of the approximations for finite QPD sizes. Figure 11 shows the effect of the limited size of a QPD on the DWS signal. In Fig. 12, the accuracy of Eqs. (57), (59) is evaluated as a function of the ratio between the QPD radius and the beam's effective spot radius, for various values of ρ. The results show that Eq. (57) accurately

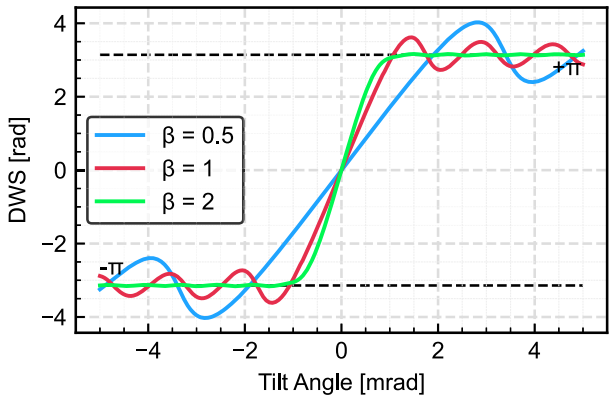

FIG. 11. Plot of the numerically calculated DWS signal for $w_{\mathrm{eff}} = 1$ mm, $\rho = 0.1$ and QPD radii of $r_{\mathrm{QPD}} = [0.5, 1, 2]/\sqrt{2}$ mm, corresponding to equivalent values of $\beta = \sqrt{2} r_{\mathrm{QPD}}/w_{\mathrm{eff}}$. To smaller values of β correspond smaller slopes around $\theta = 0$ mrad, and therefore lower sensitivity of the DWS signal; this corresponds to the plots in Fig. 12. However, this increases the range of the DWS signal, before it saturates to either $\pm\pi$. The sign reversal is also enhanced by the limited size of the QPD. This is understood to be caused by the limited number of interference fringes sensed by the QPD. In this plot, the DWS signal was unwrapped for plotting clarity.

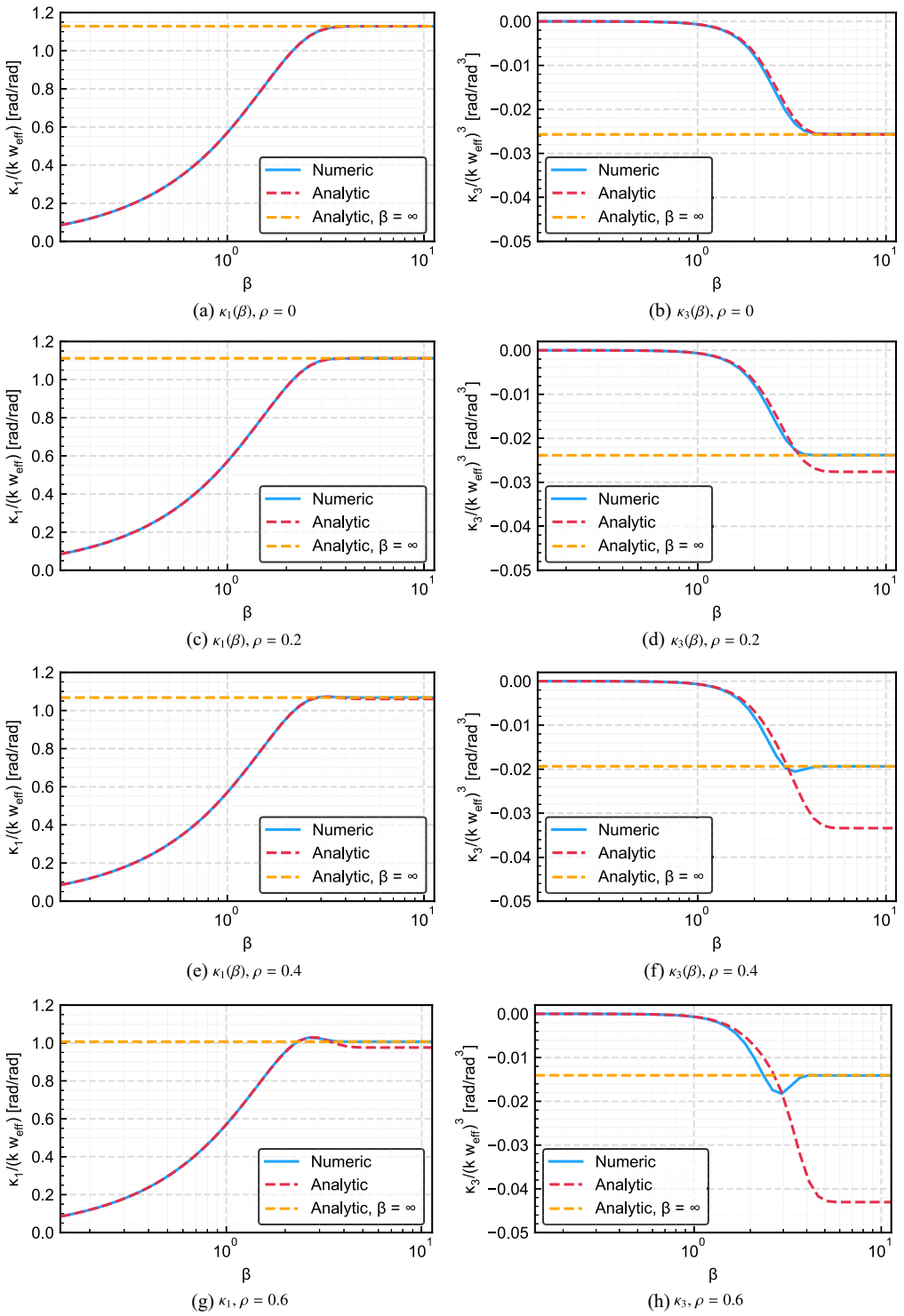

FIG. 12. Comparison between the analytically obtained parameters $\kappa_{1,\circ}$ and $\kappa_{3,\circ}$ from Eqs. (57) and (59) and the numerically calculated ones for four specific values of ρ and as a function of the parameter $\beta = \sqrt{2}r_{\mathrm{QPD}}/w_{\mathrm{eff}}$. $\kappa_{1,\circ}$ and $\kappa_{3,\circ}$ are normalized respectively by the first and third power of kw_{eff}. In subfigure (a), the analytically calculated κ_1 [using Eq. (57)] matches exactly the numerically calculated values. In subfigure (b), the analytically calculated κ_3 [using Eq. (59)] very closely matches the numerically calculated values. The approximations are surprisingly good in describing the situations with low β values. As ρ increases, the analytical approximation loses precision, with κ_3 suffering much larger deviations than κ_1. Equation (57) is a very good approximation for κ_1 up to $\rho = 0.2$, while Eq. (59) shows significant departure already at $\rho = 0.1$. The analytical approximation for $\kappa_{3,\circ}$ could potentially benefit from a further term in the expansion in ρ. This figure shows also that, as β decreases, $\kappa_{3,\circ}$ tends to zero much quicker than $\kappa_{1,\circ}$. This means that, for small values of β, the DWS signal progressively linearizes.

predicts the parameter κ_1 across all tested values of ρ and for small QPD sizes. However, for $\rho > 0.4$ and large QPD radii, small deviations begin to emerge. Similarly, while κ_3 is well-approximated by the expression for small QPD sizes, the discrepancy increases with both ρ and detector radius.

IV. DWS GAIN AND IMAGING SYSTEMS

Consider a pair of beams, i.e., a measurement beam and a reference beam, impinging on a large QPD. Both beams are nominally incident perpendicular to the detector surface; however, the measurement beam is allowed to rotate by a small angle θ about the center of the QPD. The effective beam spot radius and the relative radius of curvature (RoC) at the QPD are denoted by w_{eff} and R_{rel}, respectively. In this configuration, the resulting DWS signal is described by Eqs. (38) and (39).

Now, consider introducing a collimating imaging system: the entrance pupil of the imaging system is placed at the original position of the QPD, while the QPD itself is relocated to the exit pupil. What is the resulting DWS signal for this combined system of imaging optics and detector? The propagation of a Gaussian beam through a collimating imaging system with angular magnification m modifies the beam parameters according to Eqs. (3) and (4). These transformations apply not only to the individual beam parameters, but also to the effective beam spot radius w_{eff}, the relative radius of curvature R_{rel}, and the parameter ρ,

$$w_{\mathrm{eff,out}} = m^{-1} w_{\mathrm{eff,in}} \tag{63}$$

$$R_{\mathrm{rel,out}} = m^{-2} R_{\mathrm{rel,in}} \tag{64}$$

$$\rho_{\mathrm{out}} = \rho_{\mathrm{in}}. \tag{65}$$

An important consequence is that the parameter ρ (the effective-spot-radius-normalized wave front curvature mismatch) is invariant under propagation through a collimating imaging system. In contrast, the tilt angle θ between the beams is magnified by a factor m, as described by Eq. (2). When computing the DWS signal for such a beam configuration using an infinitely large QPD, the m factors cancel in Eq. (39). In other words, the previously mentioned quantity $\Theta = k w_{\mathrm{eff}} \theta$ is invariant under the presence of a collimating imaging system. Therefore, in the limit of small tilts and infinite detector size, the DWS signal remains unchanged in the presence of the imaging system. For a finite-sized QPD, the DWS signal remains invariant as long as the ratio $\beta = \sqrt{2} r_{\mathrm{QPD}} / w_{\mathrm{eff}}$ is conserved. However, this conclusion breaks down when the magnified tilt becomes large enough to invalidate the linear approximation in θ used in Eq. (22).

As previously discussed, the use of imaging systems in LISA is motivated by the beam compression feature, TTL suppression and beam walk suppression. This enables the use of a smaller QPD. A reduced QPD size leads to lower capacitance, which is essential for minimizing electronic noise coupling into the readout.

V. RESULTS

This section presents the DWS calibration measurements performed in TDOBS, aimed at experimentally validating the DWS model. The calibration procedure involves multiple steps, which can be broadly summarized as follows: first, the angle between the interfering beams must be accurately measured; second, the measured angle is compared against the corresponding DWS signal to establish the calibration.

A. DPS calibration

In the nominal optical layout, the beams in TDOBS are aligned to impinge orthogonally and centered on each QPD. Deviations from this ideal alignment can be detected using the differential power sensing (DPS) signal. However, the DPS signal itself requires calibration, which cannot be performed using TDOBS alone. To enable this, an external large-area QPD, mounted on micrometer translation stages, is introduced. This detector, referred to as the auxiliary QPD (AUXQPD), allows for precise calibration of the DPS signal of the Rx beams by correlating the measured signal with known displacements of the beams from the center of the AUXQPD. This procedure is illustrated in Fig. 13. The resulting calibration is subsequently applied, where feasible, to calibrate the DPS signals of the Rx beams on all other QPDs within TDOBS.

B. DWS calibration

The DWS calibration in TDOBS is performed by tilting the Rx beam about the center of the QPD under test, i.e., either the REFQPDs or the SCIQPDs, using the steering mirrors on the TS. This procedure is depicted in Fig. 14. To establish the calibration, the measured beam angle is compared with the corresponding DWS signal.

The beam angle is determined using the optical lever formed by two QPDs located at different positions along

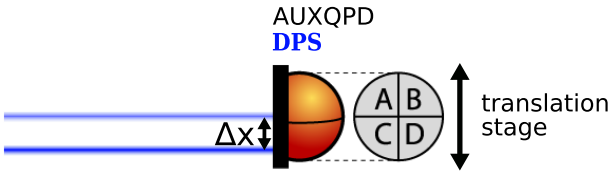

FIG. 13. Drawing of the beam translation process. The Rx beams are fixed in the propagation axis and impinge on the AUXQPD. The AUXQPD is mounted on a translation stage, which allows for vertical and horizontal displacement. The lateral displacement Δx can be related to the measured DPS signal at the AUXQPD.

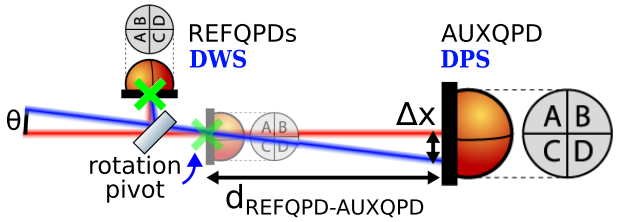

FIG. 14. Drawing of the beam rotation process. The REFQPD is located on the left, while the AUXQPD is located on the right. The virtual position of the REFQPD along the beam path is also shown in transparency. The Rx beam's rotation pivot is indicated by the green cross. The synthesized beam tilt is aligned to the axis of the QPD. The lateral displacement Δx is measured using the DPS signal of the AUXQPD. The tilt angle of the Rx beam θ can be recovered using Eq. (66). The tilt angle in the figure is strongly exaggerated; this is in the range of ± 1 mrad.

the beam path, specifically, the REFQPDs and the AUXQPD. Since the Rx beam is always kept centered on the REFQPD, the angle can be computed as

$$\theta = \frac{\Delta x_{\mathrm{AUXQPD}}}{d_{\mathrm{REFQPD\text{-}AUXQPD}}}, \tag{66}$$

where $\Delta x_{\mathrm{AUXQPD}}$ is the lateral displacement of the beam measured on the AUXQPD, and $d_{\mathrm{QPD\text{-}AUXQPD}}$ is the distance between the two QPDs along the beam path. This procedure is the main (systematic) uncertainty source of the measurement, as $d_{\mathrm{REFQPD\text{-}AUXQPD}}$ is known to within $\sim 7\%$ precision.

During the beam rotation procedure, the DPS signal readout of the Rx beam is used to actively maintain the beam centred on REFQPD1. This method, however, could not be applied to the Rx-FT beam. Due to its significantly larger size relative to the REFQPD and its flat intensity profile, the REFQPDs are effectively insensitive to the DPS signal of the Rx-FT beam. To overcome this limitation, the Rx-FT beam was rotated using only one steering mirror. In this configuration, the tilt pivot is located at the steering mirror rather than at the center of the QPD. For a plane wave, this change in pivot position is inconsequential (as discussed in [33]). Under this setup, the beam angle is determined solely using the AUXQPD, with the distance in Eq. (66) corresponding to the distance between the steering mirror and the AUXQPD. Due to this beam position control issue, the DWS signal of the Rx-FT&LO beams was calibrated only on the REFQPD, and not also on the SCIQPDs as was the case for the Rx-GB&LO beams.

This procedure introduces, however, two major issues. First, the Rx-FT beam's center must be kept within a short distance from the center of the REFQPD to maintain a clear beat note. This step is challenging, as we cannot measure the Rx-FT beam's position at the REFQPDs. Second, the portion of the Rx-FT beam being measured at the QPD during calibration varies, potentially coupling wave front errors of the Rx-FT beam into the measurement.

The resulting DWS calibrations for the Rx-GB&LO and Rx-FT&LO beam pairs are shown in Fig. 15, while the fit parameters of the calibration are reported in Table I. The beam spot radii in the experiment are approximately 1 mm radius, while the REFQPDs have radii of 0.5 mm. Under these conditions, κ_1 and κ_3 assume particularly smaller values than for an infinite QPD, as predicted by the analytical model in Fig. 12. Notice that κ_3 is more suppressed than κ_1, and therefore the DWS signal is linearized. This corresponds to an increase in the range of the DWS signal. The measured DWS signals show excellent agreement with both numerical simulations and the analytical model.

The interferometric configurations using the Rx-GB&LO beams on the REFQPDs and on the SCIQPDs differ only because of the presence of a collimating imaging system with magnification $m_{\mathrm{IS}} = 2.5$, which is exactly the case described in Sec. IV, serving as a test of its validity. As argued in this section, the values w_{eff} in the two configurations should have a ratio equal to m_{IS}, while the values of ρ should remain constant. This is exactly what we find with the data from Table I. As the size of the REFQPDs and SCIQPDs is the same, the ratio between the beta values is also m_{IS},

$$\frac{w_{\mathrm{eff,\ RxGB\text{-}LO\ @\ REFQPDs}}}{w_{\mathrm{eff,\ RxGB\text{-}LO\ @\ SCIQPDs}}} = 2.52 \pm 0.05 = m_{\mathrm{IS}} \tag{67}$$

$$\frac{\rho_{\mathrm{eff,\ RxGB\text{-}LO\ @\ REFQPDs}}}{\rho_{\mathrm{eff,\ RxGB\text{-}LO\ @\ SCIQPDs}}} = 1.0 \pm 0.01 = 1. \tag{68}$$

Furthermore, whereas the DWS gain decreases in the Rx-GB and LO @ SCIQPDs configuration with respect to the Rx-GB and LO @ REFQPDs due to the smaller beam size, the total DWS gain of the Rx-GB and LO @ SCIQPDs plus imaging system configuration exceeds that of the Rx-GB and LO @ REFQPDs configuration because of the higher value of β.

$$\kappa_{1,\ \mathrm{RxGB\text{-}LO\ @\ REFQPDs}} = 2828 \pm 5\ \mathrm{rad/rad} \tag{69}$$

$$\kappa_{1,\ \mathrm{RxGB\text{-}LO\ @\ SCIQPDs}} = 2089 \pm 14\ \mathrm{rad/rad} \tag{70}$$

$$m_{\mathrm{IS}} \cdot \kappa_{1,\ \mathrm{RxGB\text{-}LO\ @\ REFQPDs}} = 5222 \pm 35\ \mathrm{rad/rad}. \tag{71}$$

Last, the ratio between the total DWS gain of the Rx-GB and LO @ SCIQPDs and the DWS gain of the Rx-GB and LO @ REFQPDs configuration lies within 1 standard deviation from ratio predicted by the analytical model. The significance of this test lies in its independence on the systematic uncertainty in the determination of the θ angle via Eq. (66).

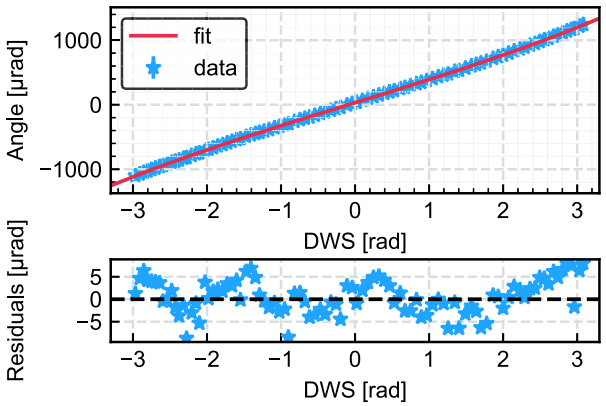

(a) Rx-GB&LO beams @ REFQPD calibration.

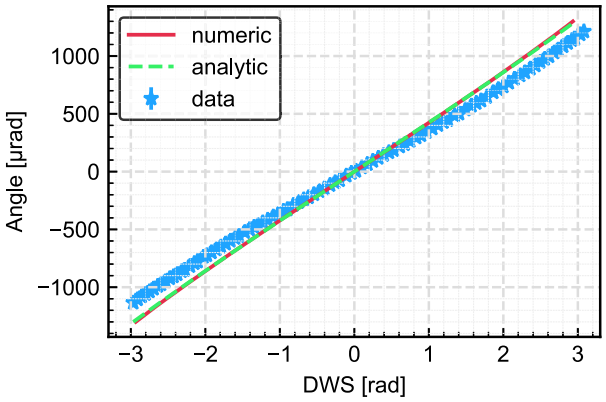

(b) Rx-GB&LO beams @ REFQPD, comparison between calibration (offset-adjusted) and model.

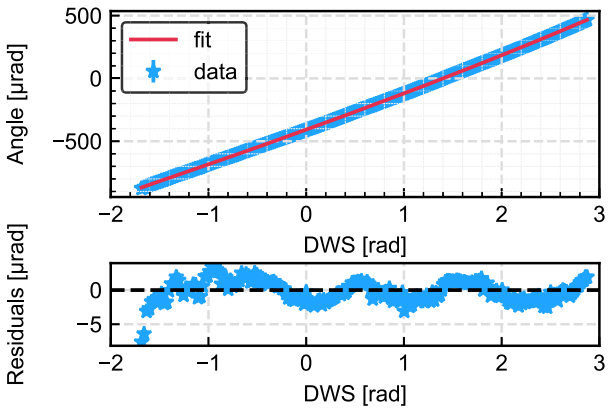

(c) Rx-FT&LO beams @ REFQPD calibration.

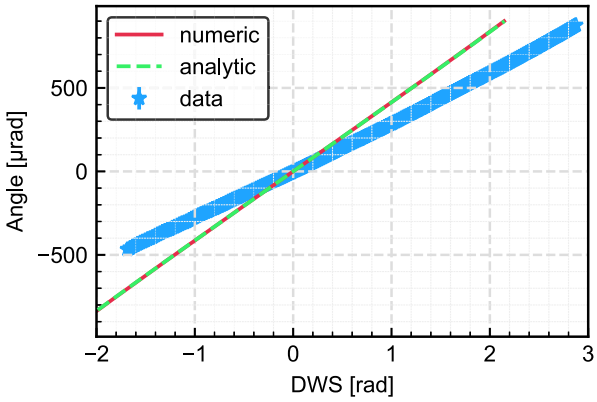

(d) Rx-FT&LO beams @ REFQPD, comparison between calibration (offset-adjusted) and model.

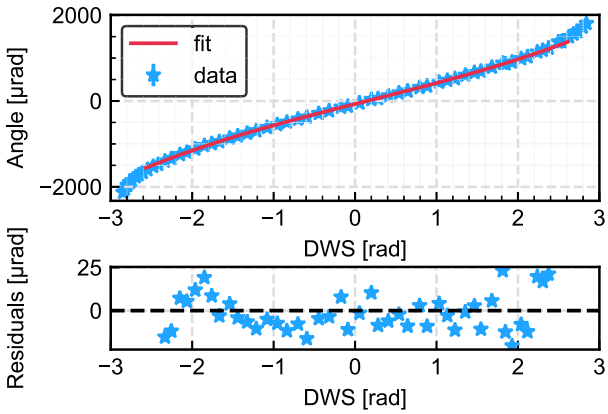

(e) Rx-GB&LO beams @ SCIQPD calibration.

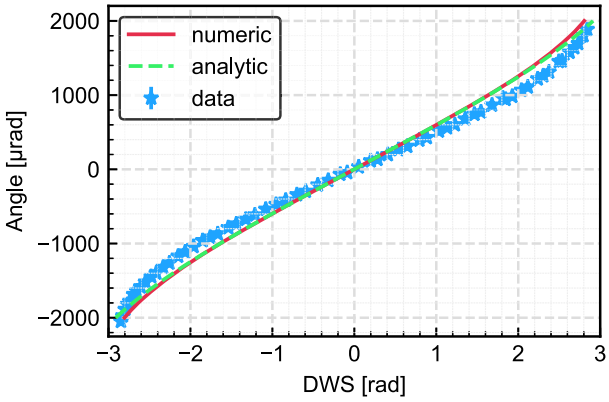

(f) Rx-GB &LO beams @ SCIQPD, comparison between calibration (offset-adjusted) and model.

FIG. 15. Left: Calibration of the DWS signal of the (a) Rx-GB and LO beams on REFQPD1, (c) Rx-FT and LO beams on REFQPD1, (e) Rx-GB and LO beams on SCIQPD1. Note that the beam angle is defined at QPD-level; this means that the beam angle at the SCIQPDs includes the magnification by the imaging systems, with an angular magnification of $m_{\mathrm{IS}} = 2.5$. The obtained data points were fitted with the function $f(x) = p_1(x - x_0) + p_3(x - x_0)^3$. The DWS parameters κ_1 and κ_3 reported in Table I are found by inverting $f(x)$. The uncertainty in the separation between the steering mirrors and the AUXQPD constitutes the main error contribution to the DWS calibration. Right: Measured DWS signal of the corresponding left subfigure plotted together with the numeric model of the DWS signal (b) Rx-GB and LO beams on REFQPD1, (d) Rx-FT and LO beams on REFQPD1, (f) Rx-GB and LO beams on SCIQPD1. In the numeric model, a GAP1000Q QPD was used (1 mm diameter, 20 μm wide insensitive slits). One can see that the numeric and analytic models are very close. The simulated DWS signals lie within the uncertainty in the geometrical parameters of the experiment, although a large discrepancy is visible for the Rx-FT and LO beams. The experimentally obtained DWS parameters are listed in Table I.

TABLE I. Beam and DWS parameters of the beams in Fig. 15. The beam parameters are derived by beam profiling the individual beams in TDOBS. The model is derived numerically. Note that the measured values of ρ for the Rx-GB and LO beams are very close, as predicted in Sec. IV. The DWS parameters are calculated by fitting the DWS signals in Fig. 15, left. The DWS signal of the Rx-GB and LO beams at the SCIQPDs refers to the signal measured specifically at the QPD, without accounting for the magnification of the imaging system. Accounting also for this, the DWS gain is $\kappa_1 = 5222 \pm 35$ rad/rad. As argued in Sec. IV, adding imaging systems gives the same DWS gain in the limit of an infinite QPD. Therefore, the increase of overall DWS gain for the SCIQPDs is due solely to the increase of the parameter β.

				Measurement		Model	
Beams and QPDs	w_{eff} [m]	ρ	β	κ_1 [rad/rad]	κ_3 [rad/rad^3]	κ_1 [rad/rad]	κ_3 [rad/rad^3]
Rx-GB and LO @ REFQPDs	0.95 ± 0.02	0.14 ± 0.01	0.74	2828 ± 5	$-(2.33 \pm 0.09) \times 10^8$	2397	-5.28×10^7
Rx-FT and LO @ REFQPDs	1.24 ± 0.01	0.34 ± 0.01	0.57	3549 ± 1	$-(9.21 \pm 0.5) \times 10^7$	3376	-1.82×10^8
Rx-GB and LO @ SCIQPDs	0.377 ± 0.002	0.14 ± 0.01	1.87	2089 ± 14	$-(2.47 \pm 0.7) \times 10^8$	1742	-6.13×10^7

$$\frac{m_{\text{IS}} \cdot \kappa_{1,\ \text{RxGB-LO @ SCIQPDs, model}}}{\kappa_{1,\ \text{RxGB-LO @ REFQPDs, model}}} = 1.796 \tag{72}$$

$$\frac{m_{\text{IS}} \cdot \kappa_{1,\ \text{RxGB-LO @ SCIQPDs, meas}}}{\kappa_{1,\ \text{RxGB-LO @ REFQPDs, meas}}} = 1.85 \pm 0.06 \tag{73}$$

A relatively large deviation is observed for the DWS signal of the Rx-FT and LO pair. The Rx-FT beam is modeled as a plane wave, corresponding to the limit $w_{\text{Rx-FT}}$, $R_{\text{Rx-FT}} = \infty$, and leading to $w_{\text{eff}} = \sqrt{2} w_{\text{LO}}$ and $|R_{\text{rel}}| = |R_{\text{LO}}|$. For this configuration, a discrepancy of approximately 17% from the model prediction is measured. We attribute this difference to the previously mentioned issues in the rotation of the Rx-FT beam. To improve this measurement, we propose to add a further QPD large enough to be sensitive to the DPS signal of the Rx-FT beam. Such a QPD could be placed in an optical copy of the Rx-clip, allowing for a correct rotation of the beam, as was done for the Rx-GB beam.

VI. TAILORING OF LISA REQUIREMENTS

This section aims to give a reference target to the experiments aiming to demonstrate LISA's stringent performance requirements. These are expressed in terms of longitudinal and angular readout noise. A direct application of them to an on-ground testbed such as TDOBS would be inaccurate and misleading for the angular requirements, as the DWS gains depend on the specific geometrical parameters of the experiment. Additionally, beam splitting for redundancy and the inclusion of imaging systems further modify the signal path, making the requirements dependent on the specific point of application within the system. This section outlines, in a step-by-step manner, the derivation of the phase stability requirements that an on-ground facility must satisfy in order to validate the DWS performance expected for LISA, while accounting for all these experimental factors.

A. The LISA requirements

The successful mitigation of TTL using the techniques outlined in the Introduction requires angular readout precision on the order of 1 nrad/$\sqrt{\text{Hz}}$. More specific requirements have been defined by the LISA team and compiled by ESA as indicative noise allocations for the mission. As of 2025, the latest update on these requirements is provided in [35]. This work focuses on the Interferometric Detection System (IDS) performance requirements for both DWS and LPS, as specified in [35] [pages 21, 24, 26, 50].

The IDS requirements are defined individually for each interferometer and are relaxed at the lower frequencies, where the total instrument noise is dominated by the TM acceleration noise. The frequency-dependent relaxation is expressed through dedicated *noise shape functions* for the LPS and DWS signals: $u_{\text{IDS}}(f)$ and $u_{\text{DWS}}(f)$,

$$u_{\text{IDS}}(f) = \sqrt{1 + \left(\frac{2\ \text{mHz}}{f}\right)^4} \tag{74}$$

$$u_{\text{DWS}}(f) = \sqrt{1 + \left(\frac{0.7\ \text{mHz}}{f}\right)^4}. \tag{75}$$

Table II lists the LPS and DWS sensitivity requirements for LISA, with the values highlighted in bold in the second column. These requirements are specified at the OB-level, meaning they refer to the beam properties immediately after the exit pupil of the telescope, excluding the effects of subsequent beam splitting or propagation through imaging systems.

The requirements also define an angular field of view (FoV) under which the DWS signal must deliver full performance in terms of both angular sensing accuracy and noise. For the Rx beam in the ISI, this range is ± 405 μrad of off-pointing angle at the OB-level. A corresponding validity range for the Tx beam in the TMI has not yet been formally defined. Note that these

TABLE II. DWS requirements for LISA reported at all levels. The at OB-level requirements are defined in [35] and reported in bold. All other values were derived during this section. The DWS ISI requirement shall be met for Rx beam off-pointing angles up to ±405 μrad at OB-level. A corresponding validity range for the Tx beam in the TMI has not yet been formally defined.

	Angle/path length			Phase			
	Level		Units	Level		Units	
Requirement	OB	QPD		QPD	seg		Noise-shape function
DWS TMI	**5**	17.7	$\mathrm{nrad}/\sqrt{\mathrm{Hz}}$	26.8	26.8	$\mu\mathrm{rad}/\sqrt{\mathrm{Hz}}$	u_{DWS}
DWS ISI	**30**	150	$\mathrm{nrad}/\sqrt{\mathrm{Hz}}$	276	276	$\mu\mathrm{rad}/\sqrt{\mathrm{Hz}}$	u_{DWS}
LPS RFI	**2**	2.8	$\mathrm{pm}/\sqrt{\mathrm{Hz}}$	16.7	33.4	$\mu\mathrm{rad}/\sqrt{\mathrm{Hz}}$	u_{IDS}
LPS TMI	**2.6**	3.7	$\mathrm{pm}/\sqrt{\mathrm{Hz}}$	21.7	43.4	$\mu\mathrm{rad}/\sqrt{\mathrm{Hz}}$	u_{IDS}
LPS ISI	**9**	18	$\mathrm{pm}/\sqrt{\mathrm{Hz}}$	106	212	$\mu\mathrm{rad}/\sqrt{\mathrm{Hz}}$	u_{IDS}

angular ranges are magnified when the beams propagate through the imaging systems.

B. Angular readout requirements

The calculations in this section assume that the main noise contributions to the QPR signals are uncorrelated, which is true for shot noise and electronic noise, but not for relative intensity noise (RIN), which introduces a small common-mode component. The impact of RIN is extensively analyzed in [30] [Table 5.2] and is sufficiently small that it can be neglected in our context.

To reach such requirement—or noise level—at the OB-level, a higher noise at the QPD-level can be allowed. First, the combination of more individual QPD measurements improves the overall SNR; this holds for both the DWS and the LPS requirements. The TMI and RFI interferometers use $n_{\mathrm{QPR,\,TMI/RFI}} = 2$ QPRs, while the ISI uses $n_{\mathrm{QPR,ISI}} = 4$. Second, the presence of imaging systems in front of the QPDs magnifies the angle between the wave fronts, hence relaxing the DWS requirement. LISA's imaging systems will have an angular magnification of $m_{\mathrm{IS}} = 2.5$ [36]. The DWS and LPS requirements at QPD-level are related to those at OB-level by Eqs. (76) and (77). This magnification also applies to the angular range of the requirements according to Eq. (78). The DWS FOV requirement at the QPD-level for the ISI is then 1 mrad. This principle is illustrated in Fig. 16. The resulting QPD-level requirements are listed in Table II, third column,

$$\mathrm{req}_{\mathrm{LPS,\,IFM,\,QPD}} = \sqrt{n_{\mathrm{QPR,IFM}}} \cdot \mathrm{req}_{\mathrm{LPS,\,IFM,\,OB}} \quad \mathrm{IFM} \in (\mathrm{ISI, TMI, RFI}) \tag{76}$$

$$\mathrm{req}_{\mathrm{DWS,\,IFM,\,QPD}} = \sqrt{n_{\mathrm{QPR,IFM}}} \cdot m_{\mathrm{IS}} \cdot \mathrm{req}_{\mathrm{DWS,\,IFM,\,OB}} \tag{77}$$

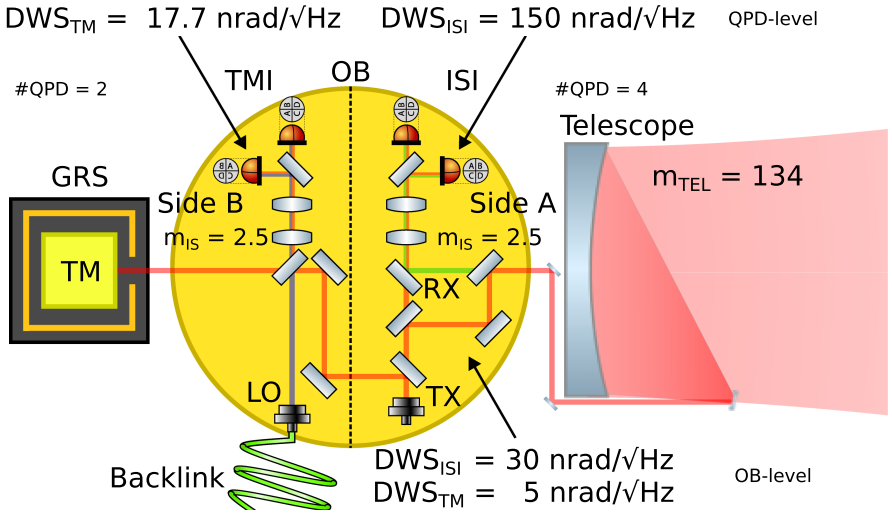

FIG. 16. Simplified scheme of the LOB. Side A, hosting the ISI, and side B, hosting the TMI [21], are here simply represented as the two halves of a circle. In each side of the LOB the respective interferometer is shown, featuring a simplified beam path, an imaging system and two quadrant photodiodes (QPDs). Only two QPRs per interferometer are shown instead of the nominal four for the ISI. The DWS requirements and their application point are shown on the drawing.

$$\mathrm{FoV}_{\mathrm{DWS,\,IFM,\,QPD}} = m_{\mathrm{IS}} \cdot \mathrm{FoV}_{\mathrm{DWS,\,IFM,\,OB}} \quad \mathrm{IFM} \in (\mathrm{ISI}, \mathrm{TMI}). \tag{78}$$

C. Phase readout requirements

The requirements at the QPD-level can be converted into phase requirements req_ϕ. The process is straightforward for the LPS requirement, as it is simply scaled by $k = \frac{2\pi}{\lambda}$. For the DWS requirements, the scaling factors are the κ_1 parameters, which depend on the geometrical properties of each interferometer. In the latest LISA design,

(i) The ISI features the interference between the Rx beam, which is a finite plane wave, and the Tx beam, which is a Gaussian beam. The TMI features the interference between the Tx and the LO beams, which are both Gaussian beams.
(ii) The Gaussian beam's (hence the Tx and LO) parameters lie in the range $0.34\ \mathrm{mm} < w_0 < 0.46\ \mathrm{mm}$ and $|z_0| < 160\ \mathrm{mm}$, with $z_0 = 0\ \mathrm{mm}$ indicating the position of the QPD. The two beams can be considered independent.
(iii) At the surface of the QPDs, the Rx beam is a flat wave front with a uniform phase and intensity profile with a diameter of $\sim 0.89\ \mathrm{mm}$. For the purpose of the following calculations, the Rx beam is parametrized as $w_{\mathrm{Rx}}, R_{\mathrm{Rx}} = \infty$.
(iv) The QPD's diameter is 1.5 mm. There are 20 μm gaps between the segments [37]. These gaps are approximately as sensitive as the QPD's active area, hence the QPD can be considered as having no gaps.

From the latest LISA design, a range of possible κ_1 values can be estimated for the TMI and the ISI; these are listed in Table III, and are divided into best and worst-case scenario based on Eq. (48). The best-case scenario corresponds to the maximum value of w_{eff} and the minimum value of $|\rho| = 0$. Conversely, the worst-case scenario is defined by the minimum value of w_{eff}, and the maximum value of $|\rho|$ within the first condition.

In the case of the ISI, an additional remark is necessary. The Rx beam's spot radius is smaller than the radius of the QPD's active area. Therefore, the area of the QPD which is illuminated solely by the Tx beam and not by the Rx beam contributes to a DC photocurrent, without any phase information, as no interference is happening. An analogous situation would be that of a reduced QPD diameter, corresponding to the size of the Rx beam.

Conservatively, the worst-case scenario value of κ_1 is used. The phase requirements for DWS can be derived using Eqs. (79) and (80). The resulting QPD-level phase requirements are listed in Table II, fifth column,

$$\mathrm{req}_{\phi\text{–LPS, IFM, QPD}} = \frac{1}{k}\mathrm{req}_{\mathrm{LPS,\,IFM,\,QPD}} \quad \mathrm{IFM} \in (\mathrm{ISI}, \mathrm{TMI}, \mathrm{RFI}) \tag{79}$$

$$\mathrm{req}_{\phi\text{-DWS, IFM, QPD}} = \kappa_{1,\mathrm{IFM,worst}}\mathrm{req}_{\mathrm{DWS,\,IFM,\,QPD}} \quad \mathrm{IFM} \in (\mathrm{ISI}, \mathrm{TMI}). \tag{80}$$

As a final step, the QPD-level phase requirements can be converted into segment-level phase requirements. This step takes into account the normalization coefficients of the DWS and LPS signals, which are $1/2$ and $1/4$, respectively, together with the assumption that the segment noises are uncorrelated. This step is formalized in Eqs. (81) and (A1). The resulting segment-level phase requirements are reported in Table II, sixth column,

$$\mathrm{req}_{\phi\text{–LPS, IFM, seg}} = 2\mathrm{req}_{\phi\text{–LPS, IFM, QPD}} \quad \mathrm{IFM} \in (\mathrm{ISI}, \mathrm{TMI}, \mathrm{RFI}) \tag{81}$$

TABLE III. Parameters of the TMI and ISI in LISA. The values of w_{eff}, ρ, r_{QPD} and β are listed. Note that both the TMI and the ISI use the same QPR model with radius $r_{\mathrm{QPD}} = 0.75$ mm, but the effective QPD radius in the case of the ISI is reduced to the radius of the Rx beam. From these values, the κ_1 and κ_3 coefficients are calculated for a finite QPD with Eqs. (57) and (59) (denoted by ∘) and b) for a LISA's QPDs using numerical integration (denoted by #). The results are split into best and worst scenarios. The parameter dominating the DWS gain output is w_{eff}. Note that, in the case of the ISI, the limited effective r_{qpd} effects are noticeable (compare to Fig. 12). Also note that maximum value of ρ allowed by the beams' parameter space is $|\rho| = 0.469$ [30], which is higher than that of the worst-case scenario.

		TMI		ISI	
Parameter	Unit	Best	Worst	Best	Worst
w_{eff}	mm	0.475	0.339	0.672	0.481
$\lvert\rho\rvert$	⋯	0	0.38	0	0.38
$r_{\mathrm{QPD,eff}}$	mm	0.75	0.75	0.445	0.445
β		2.23	3.13	0.937	1.31
$\kappa_{1,\circ}$	rad/rad	2212	1514	2033	1844
$\kappa_{3,\circ}$	rad/rad^3	-1.66×10^8	-9.02×10^7	-3.82×10^7	-4.29×10^7
$\kappa_{1,\#}$	rad/rad	2213	1521	2062	1868
$\kappa_{3,\#}$	rad/rad^3	-1.74×10^8	-5.67×10^7	-6.77×10^7	-7.00×10^7

$$\mathrm{req}_{\phi\text{-DWS, IFM, seg}} = \mathrm{req}_{\phi-\text{DWS, IFM, seg}} \quad \mathrm{IFM} \in (\mathrm{ISI}, \mathrm{TMI}). \tag{82}$$

VII. SUMMARY AND CONCLUSION

The coupling of angular jitter into the interferometrically measured path length is a critical aspect for space-based interferometers such as LISA. To mitigate this issue, LISA employs an angular readout technique known as DWS. This enables LISA to actively control the tilts of the test masses and to subtract spurious path length contributions due to tilt via postprocessing.

The calibration of the DWS signal into an angular readout is a nontrivial function of the interferometer's geometry. The relationship between the measured DWS signal and the tilt angle is approximately linear for small tilts; however, nonlinearities arise at larger tilt angles within LISA's operational range. This regime can be described analytically in the limit where the QPD is much larger than the beam waist. However, this assumption does not hold for LISA, where the two sizes are comparable.

In this paper, we proposed an approximate analytical model of the DWS signal. This model is derived by performing a Maclaurin expansion of the intensity of the superimposed beams. To extract the phase, a further Taylor expansion around the wave front curvature mismatch is carried out. The resulting expression yields the first two nonzero coefficients of the Maclaurin expansion of the DWS signal for any beam geometry and a finite QPD. The derived equations are also applicable to LISA's Rx beam by setting its waist size to infinity. These analytical results were validated against numerical integration and show excellent agreement for small wave front curvature mismatches. The model was further tested against three DWS calibration campaigns performed on the ultrastable testbed described in Sec. II.

In the last section, the model is used to derive the performance requirements a testbed must meet to demonstrate LISA's DWS sensitivity. While the required path length sensitivity is trivial, being determined solely by the wavelength of the laser beams, the DWS signal is sensitive to the full interferometer geometry. Using LISA design parameters, we derived worst-case phase noise requirements for both the TMI and ISI. These requirements are detailed at the OB-level, QPD-level, and QPD-segment-level for both LPS and DWS. We hope that the results of this paper will facilitate the calculation of the DWS gain of interferometric setups of any topology and give a reference target to all the experiments aiming to demonstrate LISA's performance requirement. Future developments of this framework could further analyse not the phase, but the amplitude of the beat note generated by two beams on a PD, i.e. the heterodyne efficiency, as this is relevant for the phase noise coupling.

ACKNOWLEDGMENTS

We gratefully acknowledge support by the Deutsches Zentrum für Luft- und Raumfahrt (DLR) with funding of the Bundesministerium für Wirtschaft und Klimaschutz with a decision of the Deutsche Bundestag (DLR Project Reference No. FKZ 50 OQ 1801) and No. FKZ 50OQ2301. Additionally, we acknowledge funding by the European Space Agency within the project "Optical Bench Development for LISA" (22331/09/NL/HB), support from UK Space Agency, University of Glasgow, Scottish Universities Physics Alliance (SUPA).

DATA AVAILABILITY

The data that support the findings of this article are not publicly available upon publication because it is not technically feasible and/or the cost of preparing, depositing, and hosting the data would be prohibitive within the terms of this research project. The data are available from the authors upon reasonable request.

APPENDIX

$$\begin{aligned}
\kappa_{1,\circ,\rho-2} &= \frac{k w_{\mathrm{eff}}}{2^{\frac{3}{2}}\pi(1-e^{-\beta^2})}\sum_{n=0}^{3} e^{-n\beta^2}\tau_n \\
\tau_0 &= -3\sqrt{\pi}\,\mathrm{erf}(\beta) \\
\tau_1 &= +6\beta + 4\beta^3 + 8\beta^5 + \sqrt{\pi}\,\mathrm{erf}(\beta)(6 - 4\beta^2 - 4\beta^4) \\
\tau_2 &= -12\beta + 8\beta^5 + \sqrt{\pi}\,\mathrm{erf}(\beta)(-3 + 4\beta^2 - 4\beta^4) \\
\tau_3 &= 6\beta - 4\beta^3
\end{aligned} \tag{A1}$$

$$\begin{aligned}
\kappa_{3,\circ,\rho-0} &= \frac{\sqrt{2}(k w_{\mathrm{eff}})^3}{9\pi^3(1-e^{-\beta^2})^3}\sum_{n=0}^{3} e^{-n\beta^2}\tau_n \\
\tau_0 &= +3\pi^{5/2}\mathrm{erf}(\beta) - 12\pi^{3/2}\mathrm{erf}(\beta)^3 \\
\tau_1 &= \pi^2(-6\beta + 8\beta^3) - \pi^{5/2}\mathrm{erf}(\beta)(6 + 9\beta^2) + 72\pi\beta\,\mathrm{erf}(\beta)^2 \\
\tau_2 &= \pi^2(12\beta + 2\beta^3) - 144\sqrt{\pi}\beta^2\mathrm{erf}(\beta) + \pi^{5/2}\mathrm{erf}(\beta)(3 + 9\beta^2) \\
\tau_3 &= 96\beta^3 - \pi^2(6\beta + 10\beta^3)
\end{aligned} \tag{A2}$$

$$
\begin{aligned}
\kappa_{3,\circ,\rho-2} &= \frac{\sqrt{2}(kw_{\mathrm{eff}})^3}{72\pi^3(1-e^{-\beta^2})^5}\sum_{n=0}^{5} e^{-n\beta^2}\tau_n \\
\tau_0 &= -45\pi^{5/2}\mathrm{erf}(\beta) + 180\pi^{3/2}\mathrm{erf}(\beta)^3 \\
\tau_1 &= \pi^2(90\beta + 60\beta^3 + 24\beta^5 - 32\beta^7) - \pi\mathrm{erf}(\beta)^2(1080\beta + 720\beta^3 + 288\beta^5) + \pi^{3/2}\mathrm{erf}(\beta)^3(-360 + 432\beta^2 + 144\beta^4) \\
&\quad + \pi^{5/2}\mathrm{erf}(\beta)(+180 - 9\beta^2 + 24\beta^4 + 36\beta^6) \\
\tau_2 &= -\pi^2(360\beta + 222\beta^3 + 132\beta^5 + 256\beta^7) + \pi\mathrm{erf}(\beta)^2(2160\beta - 1152\beta^3 - 2016\beta^5) \\
&\quad + \pi^{3/2}\mathrm{erf}(\beta)^3(180 - 432\beta^2 + 432\beta^4) + \pi^{5/2}\mathrm{erf}(\beta)(-270 + 27\beta^2 - 24\beta^4 + 108\beta^6) \\
&\quad + \sqrt{\pi}\mathrm{erf}(\beta)(2160\beta^2 + 2880\beta^4 + 2304\beta^6) \\
\tau_3 &= -1440\beta^3 - 2880\beta^5 - 3456\beta^7 + \pi^2(540\beta + 306\beta^3 + 156\beta^5 + 176\beta^7) + \pi\mathrm{erf}(\beta)^2(-1080\beta + 1872\beta^3 - 1152\beta^5) \\
&\quad + \pi^{5/2}\mathrm{erf}(\beta)(180 - 27\beta^2 - 24\beta^4 - 108\beta^6) + \sqrt{\pi}\mathrm{erf}(\beta)(-4320\beta^2 - 576\beta^4 + 4032\beta^6) \\
\tau_4 &= 2880\beta^3 + 2304\beta^5 - 1152\beta^7 + \pi^2(-360\beta - 186\beta^3 - 12\beta^5 + 112\beta^7) + \pi^{5/2}\mathrm{erf}(\beta)(-45 + 9\beta^2 + 24\beta^4 - 36\beta^6) \\
&\quad + \sqrt{\pi}\mathrm{erf}(\beta)(2160\beta^2 - 2304\beta^4 + 576\beta^6) \\
\tau_5 &= -1440\beta^3 + 576\beta^5 + \pi^2(90\beta + 42\beta^3 - 36\beta^5)
\end{aligned}
\tag{A3}
$$

[1] G. Pizzella, Eur. Phys. J. H **41**, 267 (2016).
[2] G. E. Moss, L. R. Miller, and R. L. Forward, Appl. Opt. **10**, 2495 (1971).
[3] R. Weiss, Gen. Relativ. Gravit. **54**, 153 (2022).
[4] B. P. Abbott *et al.* (LIGO Scientific and Virgo Collaborations), Phys. Rev. Lett. **116**, 061102 (2016).
[5] M. Branchesi, M. Maggiore, D. Alonso, C. Badger, B. Banerjee, F. Beirnaert, E. Belgacem, S. Bhagwat, G. Boileau, S. Borhanian *et al.*, J. Cosmol. Astropart. Phys. 07 (2023) 068.
[6] M. Evans, A. Corsi, C. Afle, A. Ananyeva, K. G. Arun, S. Ballmer, A. Bandopadhyay, L. Barsotti, M. Baryakhtar, E. Berger *et al.*, arXiv:2306.13745.
[7] M. G. Beker, J. F. J. v. d. Brand, E. Hennes, and D. S. Rabeling, J. Phys. Conf. Ser. **363**, 012004 (2012).
[8] ESA, Capturing the ripples of spacetime: LISA gets go-ahead (2024), https://www.esa.int/Science_Exploration/Space_Science/LISA/Capturing_the_ripples_of_spacetime_LISA_gets_go-ahead.
[9] M. Armano, H. Audley, G. Auger, J. T. Baird, M. Bassan, P. Binetruy, M. Born, D. Bortoluzzi, N. Brandt, M. Caleno *et al.*, Phys. Rev. Lett. **116**, 231101 (2016).
[10] M. Armano, H. Audley, J. Baird, P. Binetruy, M. Born, D. Bortoluzzi, E. Castelli, A. Cavalleri, A. Cesarini, A. M. Cruise *et al.*, Phys. Rev. Lett. **120**, 061101 (2018).
[11] G. Wanner, Nat. Phys. **15**, 200 (2019).
[12] K. Danzmann, T. Prince (The LISA Internatinal Science Team), Assessment study report (yellow book) (2011), https://sci.esa.int/documents/35005/36499/1567258681608-LISA-YellowBook-ESA-SRE-2011-3-Feb2011.pdf.
[13] W. Brzozowski, D. Robertson, E. Fitzsimons, H. Ward, J. Keogh, A. Taylor, M. Milanova, M. Perreur-Lloyd, Z. Ali, A. Earle *et al.*, in *Space Telescopes and Instrumentation 2022: Optical, Infrared, and Millimeter Wave*, edited by L. E. Coyle, S. Matsuura, and M. D. Perrin, International Society for Optics and Photonics Vol. 12180 (SPIE, 2022), p. 121800O, 10.1117/12.2627465.
[14] A.-M. A. van Veggel and C. J. Killow, Adv. Opt. Technol. **3**, 293 (2014).
[15] M. Tinto, D. A. Shaddock, J. Sylvestre, and J. W. Armstrong, Phys. Rev. D **67**, 122003 (2003).
[16] G. Wanner and N. Karnesis (LISA Pathfinder Collaboration), J. Phys. Conf. Ser. **840**, 012043 (2017).
[17] M. Tröbs, S. Schuster, M. Lieser, M. Zwetz, M. Chwalla, K. Danzmann, G. F. Barránco, E. D. Fitzsimons, O. Gerberding, G. Heinzel *et al.*, Classical Quantum Gravity **35**, 105001 (2018).
[18] M. Chwalla, K. Danzmann, M. D. Alvarez, J. E. Delgado, G. F. Barranco, E. Fitzsimons, O. Gerberding, G. Heinzel, C. Killow, M. Lieser *et al.*, Phys. Rev. Appl. **14**, 014030 (2020).
[19] M.-S. Hartig, S. Paczkowski, M. Hewitson, G. Heinzel, and G. Wanner, Phys. Rev. D **111**, 043048 (2025).
[20] M. Chwalla, K. Danzmann, G. F. Barranco, E. Fitzsimons, O. Gerberding, G. Heinzel, C. J. Killow, M. Lieser, M. Perreur-Lloyd, D. I. Robertson *et al.*, Classical Quantum Gravity **33**, 245015 (2016).

[21] M. Colpi, K. Danzmann, M. Hewitson, K. Holley-Bockelmann, P. Jetzer, G. Nelemans, A. Petiteau, D. Shoemaker, C. Sopuerta, R. Stebbins *et al.*, arXiv:2402.07571.
[22] V. Huarcaya, M. D. Álvarez, D. Penkert, S. Gozzo, P. M. Cano, K. Yamamoto, J. J. E. Delgado, M. Mehmet, K. Danzmann, and G. Heinzel, Phys. Rev. Appl. **20**, 024078 (2023).
[23] E. A. Donley, T. P. Heavner, F. Levi, M. O. Tataw, and S. R. Jefferts, Rev. Sci. Instrum. **76**, 063112 (2005).
[24] G. Fernandez Barranco, Ph.D. thesis, Leibniz Universität Hannover, 2017, 10.15488/3866.
[25] G. Fernández Barranco, B. S. Sheard, C. Dahl, W. Mathis, and G. Heinzel, IEEE Sens. J. **18**, 7414 (2018).
[26] A. Siegman, *Lasers* (University Science Books, 1986), ISBN 9780685055953, https://books.google.de/books?id=qBBaDQEACAAJ.
[27] O. Gerberding, C. Dahl, J. Kullmann, M. Tröbs, I. Bykov, S. Barke, N. Brause, J. J. Esteban Delgado, T. Schwarze, J. Reiche *et al.*, Rev. Sci. Instrum. **86**, 074501 (2015).
[28] O. Gerberding, Ph.D. thesis, Leibniz Universität Hannover, 2014, 10.15488/8255.
[29] C. Bode, Ph.D. thesis, Leibniz Universität Hannover, 2024, 10.15488/17997.
[30] A. Pizzella, Ph.D. thesis, Leibniz Universität Hannover, 2025, 10.15488/18487.
[31] E. Morrison, B. J. Meers, D. I. Robertson, and H. Ward, Appl. Opt. **33**, 5041 (1994).
[32] E. Morrison, B. J. Meers, D. I. Robertson, and H. Ward, Appl. Opt. **33**, 5037 (1994).
[33] G. Hechenblaikner, J. Opt. Soc. Am. A **27**, 2078 (2010).
[34] G. Heinzel, M. D. Álvarez, A. Pizzella, N. Brause, and J. J. E. Delgado, Phys. Rev. Appl. **14**, 054013 (2020).
[35] ESA-LISA-EST-ISD-RS-0002 LISA IDS System and Interface Requirement Document (IDS-IRD) (2024).
[36] E. Fitzsimons, M. Hewitson, A. Uminska, and G. Fernandez Barranco, IDS Performance Budgets (2024).
[37] T. Mistry, The eyes of LISA (2024), https://app.oxfordabstracts.com/content/events/5189/submitters/405298/submissions/fe-412377de-ee7f-408e-849d-84ca70d81af8/questions/91860/file/e18cb94a-84d5-4284-b64f-39c13cb08bb4.pdf.

Correction: Typographical errors in Eqs. (9), (36) and (37) have been fixed.